



## RESEARCH ARTICLE

10.1002/2013JC009373

## Key Points:

- Wave setup on fringing reefs exhibits tidal dependence
- The tidal dependence is due in part to a variable ratio of breaking wave height to water depth
- Water level changes in general are expected to have a similar effect on setup

## Correspondence to:

J. M. Becker,  
jbecker@soest.hawaii.edu

## Citation:

Becker, J. M., M. A. Merrifield, and M. Ford (2014), Water level effects on breaking wave setup for Pacific Island fringing reefs, *J. Geophys. Res. Oceans*, 119, 914–935, doi:10.1002/2013JC009373.

Received 23 AUG 2013

Accepted 12 JAN 2014

Accepted article online 16 JAN 2014

Published online 12 FEB 2014

Corrected 30 NOV 2015

This article was corrected on 30 NOV 2015. See the end of the full text for details.

## Water level effects on breaking wave setup for Pacific Island fringing reefs

J. M. Becker<sup>1</sup>, M. A. Merrifield<sup>2</sup>, and M. Ford<sup>3</sup>

<sup>1</sup>Department of Geology and Geophysics, University of Hawaii at Manoa, Honolulu, Hawaii, USA, <sup>2</sup>Department of Oceanography, University of Hawaii at Manoa, Honolulu, Hawaii, USA, <sup>3</sup>School of Environment, University of Auckland, Auckland, New Zealand

**Abstract** The effects of water level variations on breaking wave setup over fringing reefs are assessed using field measurements obtained at three study sites in the Republic of the Marshall Islands and the Mariana Islands in the western tropical Pacific Ocean. At each site, reef flat setup varies over the tidal range with weaker setup at high tide and stronger setup at low tide for a given incident wave height. The observed water level dependence is interpreted in the context of radiation stress gradients specified by an idealized point break model generalized for nonnormally incident waves. The tidally varying setup is due in part to depth-limited wave heights on the reef flat, as anticipated from previous reef studies, but also to tidally dependent breaking on the reef face. The tidal dependence of the breaking is interpreted in the context of the point break model in terms of a tidally varying wave height to water depth ratio at breaking. Implications for predictions of wave-driven setup at reef-fringed island shorelines are discussed.

### 1. Introduction

The vulnerability of low lying islands and atolls to ocean inundation is of increasing concern given sea level rise projections [Solomon *et al.*, 2007]. An area of active study involves assessing changes in the frequency and severity of extreme water level events for higher global mean sea levels [Hunter, 2012]. Factors that contribute to extreme events include storm surge, peak astronomical tides, regional sea level changes, for example, associated with the El Niño/Southern Oscillation, and the arrival of wave events from distant storms [Seneviratne *et al.*, 2012]. While most of these processes are independent of background sea level and can be assessed separately in projection estimates, the impact of breaking waves on island coastal inundation can depend on background water level, particularly when shallow coastal reefs are present [Tait, 1972; Gourlay, 1996b]. In this study, we consider the impact of tidal elevation changes on wave setup, with the underlying motivation of understanding how sea level change in general impacts coastal inundation at reef-fringed island shorelines.

Wave setup is the mean elevation in water level within and shoreward of the surf zone resulting from the excess momentum flux in the water column due to wave breaking. Field measurements on sandy beaches have shown that setup generally scales as 20–30% of the deep water significant wave height [e.g., Guza and Thornton, 1981; Nielsen, 1988]. Longuet-Higgins and Stewart [1962] showed that setup,  $\bar{\eta}$ , obeys a steady state, inviscid, cross-shelf momentum balance, assuming longshore uniform waves and bathymetry,

$$\frac{dS_{xx}}{dx} + \rho g(\bar{\eta} + h) \frac{d\bar{\eta}}{dx} = 0, \quad (1)$$

where  $S_{xx}$  is the radiation stress in the cross-shore  $x$  direction,  $\rho$  is the water density,  $g$  is the gravitational acceleration, and  $h$  is the mean water depth in the absence of waves. Solutions to (1) typically relate setup to the ratio of wave height,  $H$ , to total water depth,  $\bar{h}$ , after breaking [Bowen *et al.*, 1968],

$$\gamma \equiv \frac{H}{\bar{h}}. \quad (2)$$

Setup has been observed to exhibit tidal dependence in field studies on sand beaches [Holman and Sallenger, 1985; Raubenheimer *et al.*, 2001]. Raubenheimer *et al.* [2001] developed an empirical relationship between shoreline setup and the ratio of average surf zone depth and width, which was found to modulate

This is an open access article under the terms of the Creative Commons Attribution-NonCommercial-NoDerivs License, which permits use and distribution in any medium, provided the original work is properly cited, the use is non-commercial and no modifications or adaptations are made.

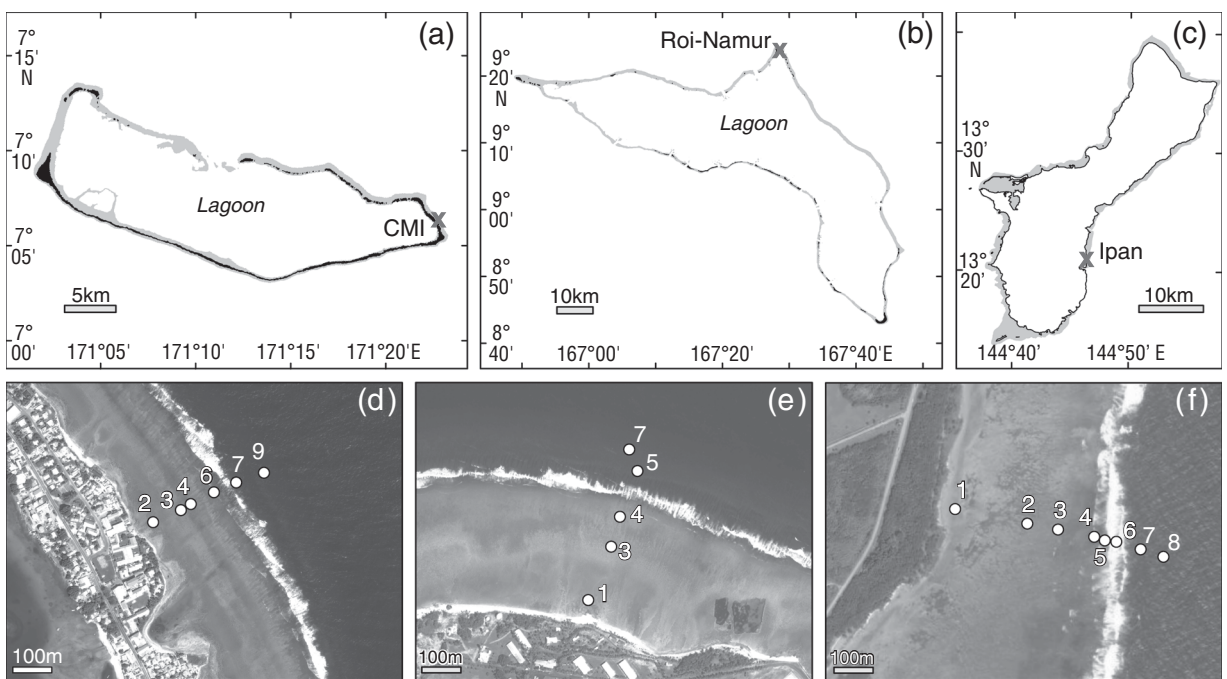
with the tidal cycle. In the case of barred beaches, tidal modulation of setup also has been attributed to increased wave dissipation over the sand bar at low tide compared to high tide [Holman and Sallenger, 1985; Raubenheimer *et al.*, 2001]. Although bottom friction generally is not included in (1), Apotsos *et al.* [2007] found that the neglect of bottom stress can lead to the underprediction of setup in field measurements.

Laboratory [Gerritsen, 1980; Seelig, 1983; Gourlay, 1996a; Nwogu and Demirbilek, 2010; Yao *et al.*, 2012] and field observations [Lugo-Fernandez *et al.*, 1998; Hearn, 1999; Hench *et al.*, 2008; Vetter *et al.*, 2010; Taebi *et al.*, 2011; Monismith *et al.*, 2013] have shown that wave-driven setup over fringing reefs behaves similarly to that over a sandy beach. One difference between the two morphologies is that fringing reefs typically include a shallow platform shoreward of the surf zone where radiation stress gradients are weak. Tait [1972] applied the result of Bowen *et al.* [1968] to a linearly sloping reef face fronting a reef flat and showed that reef flat setup is proportional to the water level at breaking. Tait [1972] also showed that reef flat setup may be reduced at high tide as depth-limited reef flat wave heights increase, which in turn weakens the radiation stress gradient forcing in (1). The opposite occurs at low tide. Similar reef flat water level effects on coral reef setup have been described in laboratory experiments [Gerritsen, 1980; Gourlay, 1996a; Yao *et al.*, 2012], and in field observations [Symonds *et al.*, 1995; Hearn, 1999]. The theory of Tait [1972] assumes a constant  $\gamma$  in the range 1–2 across the surf zone. Gourlay [1996a] and Hearn [1999] used a smaller value for  $\gamma$  on the reef flat, consistent with various field studies [e.g., Young, 1989; Hardy and Young, 1996]. Gourlay [1996b] assumed that wave breaking occurs at a characteristic depth proportional to reef flat water level, with the proportionality factor related to reef profile shape. Vetter *et al.* [2010] examined setup over a fringing reef at Ipan, Guam and showed that the dynamics of (1) and an idealized point break model of wave transformation accounted for the observed setup on the reef flat. Vetter *et al.* [2010] did not consider the effects on setup of tidal height over the reef at Ipan, in part, because the tidal range is relatively small at this location.

Since the study of Vetter *et al.* [2010], additional observations of waves and water level have been collected at Guam and at two other fringing reefs on the atoll islands of Majuro and Roi-Namur in the Republic of the Marshall Islands (RMI). The tidal range is twice as large at the RMI sites than at Guam, which provides an opportunity to study wave-driven setup over a wider range of water levels than considered in Vetter *et al.* [2010]. In addition, the reef flat widths and reef face slopes differ at the three sites. Tidally dependent setup is observed at all locations, which increases in amplitude with increasing wave height. The observed tidal dependence is due in part to the water level influence on reef flat wave heights as described in the aforementioned reef studies, but not entirely so. We revisit the point break model of Vetter *et al.* [2010], extended for nonnormally incident waves, and find that the tidal dependence of the breaking wave setup may be attributed in part to a water level dependent  $\gamma$  at the assumed point break. Although more realistic models of wave transformations over fringing reefs have been considered [e.g., Gerritsen, 1980; Massel and Gourlay, 2000; Nwogu and Demirbilek, 2010; Su *et al.*, 2011; Van Dongeren *et al.*, 2013], the simplified analytical approach presented here explains a considerable fraction of the observed setup variability at each site, and provides a useful tool for diagnosing tidally dependent setup. Factors that might contribute to the depth-dependent breaking on the reef face are considered, and major conclusions are summarized.

## 2. Field Experiment and Data

The three island and atoll study sites are located in the western tropical Pacific Ocean. The first two sites are island atolls in the RMI. Site 1 is located on Majuro atoll (Figure 1a), approximately 400 km southeast of Kwajalein. A sensor array, aligned 50°N (N is true north and positive angles are clockwise throughout), was deployed on the fringing reef adjacent to the College of the Marshall Islands (CMI) (Figure 1d). The CMI reef flat is ~250 m wide adjacent to a shoreline that has been armored through the construction of revetment and large block seawalls. The reef flat is composed of a laterally discontinuous raised conglomerate platform extending ~20 m offshore from the toe of the seawall. The remainder of the reef flat is composed of a hard, flat substrate, coated by macro-algae, and cyanobacteria with an average depth of ~0.8 m on the midreef flat (Figure 2a and Table 1). The outer sections of the reef flat include an irregular, shallow, moat zone, with small colonies of living branching and encrusting corals. Immediately seaward of the moat is the reef crest consisting of a raised algal rim. The offshore bathymetry at CMI was obtained from diver surveys.



Includes material © 2013 DigitalGlobe, Inc. ALL RIGHTS RESERVED

**Figure 1.** Maps of the experiment sites at (a) College of the Marshall Islands (CMI), Majuro atoll, RMI, (b) Roi-Namur, Kwajalein atoll, RMI, and (c) Ipan, Guam, with the transect locations indicated by a gray X. Plots (d) and (e) present ©DigitalGlobe, Inc. satellite images showing the cross-reef transects (d) and (e) at each site, respectively, with the instrument locations numbered (see Table 1).

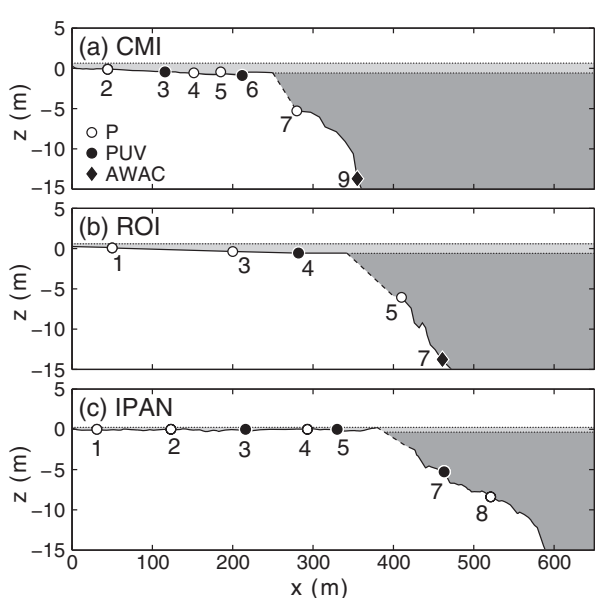


**Figure 2.** The reef bathymetry and sensor locations (P—Sea-Bird SBE26plus, PUV—Aquadopp, AWAC) for (a) CMI, (b) Roi, and (c) Ipan are presented as a function of cross-shore distance ( $x$ , positive offshore). During deployment A/a at CMI, the midreef Seabird (MA/a5) is located between sensors MC6 and MC4 (see Table 1). The dashed sections of the bathymetry curves indicate locations where wave conditions prevented direct depth measurements and linear interpolation between known points is made. The band of water levels at the surface represents mean lower low water (MLLW, bottom of light band) and mean higher high water (MHHW, top of light band), computed for the duration of the C (CMI and Roi) and L (Ipan) deployments.

Turbulence in the surf zone prevented mapping of this region (dashed curve in Figure 2a). The steep initial dropoff at the reef edge is specified as a linear slope between the shallowest diver depth measurement and the position of the offshore edge of the reef platform based on satellite images and appears to be the steepest of the three study sites (~0.16). Spur and grooves extend from the reef crest, with some grooves protruding landward through the algal rim. CMI has the densest reef face coral coverage of the three sites. Near sensor 9, the reef face drops off steeply into oceanic waters.

Site 2 is located on Kwajalein (Figure 1b), the largest atoll in the Marshall Islands. A cross-shore instrument array aligned along  $20^{\circ}\text{N}$  (Figure 1e) was deployed on the north side of Roi at the northern tip of Kwajalein (Figure 1b). Roi-Namur is composed of two islands that were connected by landfill before World War II. The fringing reef at Roi includes a ~0.8 m deep at midreef, ~350 m wide, gently sloping (0.009) platform that extends from a narrow sandy shore to a slightly raised reef

**Table 1.** Details of the Sensor Deployments for Each of the Study Sites<sup>a</sup>

Sensor	Type	Depth	Position	Burst Sample	Site and Time
MA2 (s)	P	0.4 m	44 m	2/4 h	CMI, Dec 2009 to Feb 2010
MA5 (r)	P	0.8 m	185 m	2/4 h	
MA7 (f)	P	5.2 m	280 m	2/4 h	
Ma2 (s)	P	0.5 m	44 m	2/4 h	CMI, Feb 2010 to May 2010
Ma5 (r)	P	1.0 m	185 m	2/4 h	
Ma7 (f)	P	4.7 m	260 m	2/4 h	
MC2 (s)	P	0.5 m	44 m	1.5/3 h	CMI, Nov 2010 to Mar 2011
MC3	PUV	0.7 m	115 m	1.5/3 h	
MC4 (r)	P	0.8 m	152 m	1.5/3 h	
MC6	PUV	1.0 m	212 m	1.5/3 h	
MC7 (f)	P	5.3 m	280 m	1.5/3 h	
MC9 (o)	AUV	13.8 m	355 m	0.21/1 h	
RC1 (s)	P	0.4 m	50 m	1.5/3 h	Roi, Nov 2010 to Jan 2011
RC3 (r)	P	0.7 m	200 m	1.5/3 h	
RC4	PUV	0.8 m	282 m	1.5/3 h	
RC5 (f)	P	6.0 m	410 m	1.5/3 h	
RC7 (o)	AUV	13.8 m	461 m	0.21/1 h	
Rc1 (s)	P	0.5 m	50 m	1.5/3 h	Roi, Jan 2011 to May 2011
Rc3 (r)	P	0.7 m	200 m	1.5/3 h	
Rc4	PUV	0.9 m	282 m	1.5/3 h	
Rc5 (f)	P	6.1 m	410 m	1.5/3 h	
Rc7 (o)	AUV	13.8 m	461 m	0.21/1 h	
IL1 (s)	P	0.5 m	30 m	2/4 h	Ipan, Dec 2008 to Feb 2009
IL2	P	0.5 m	195 m	2/4 h	
IL3 (r)	PUV	0.5 m	277 m	1.5/4 h (0.2:0.1 m)	
IL4	P	0.7 m	359 m	2/4 h	
IL5	PUV	0.7 m	396 m	1.5/4 h (0.2:0.1 m)	
IL7	PUV	5.8 m	475 m	1.5/4 h (0.2:1.6 m)	
IL8 (f)	P	8.0 m	530 m	2/4 h	
IN1 (s)	PUV	0.4 m	30 m	3/4 h (0.2:0.1 m)	Ipan, Sep 2009 to Nov 2009
IN2	P	0.4 m	195 m	11.99/12 h	
IN3 (r)	PUV	0.3 m	277 m	3/4 h (0.2:0.1 m)	
IN5	PUV	0.6 m	396 m	3/4 h (0.2:0.1 m)	
IN6	P	0.2 m	416 m	11.99/12 h	
IN7	PUV	5.8 m	475 m	3/4 h (1:1 m)	
IN8 (f)	PUV	7.9 m	530 m	3/4 h (1:1 m)	
IO1 (s)	PUV	0.4 m	30 m	1.5/4 h (0.2:0.1 m)	Ipan, Dec 2009 to May 2010
IO2	P	0.4 m	195 m	1.5/4 h	
IO3 (r)	PUV	0.3 m	277 m	1.5/4 h (0.2:0.1 m)	
IO5	PUV	0.5 m	396 m	1.5/4 h (0.2:0.1 m)	
IO6	P	0.2 m	416 m	1.5/4 h	
IO7	PUV	5.7 m	475 m	1.5/4 h (1:1 m)	
IO8 (f)	PUV	7.9 m	530 m	1.5/4 h (1:1 m)	

<sup>a</sup>Sensor: First symbol indicates site (M—CMI, R—ROI, I—Ipan), second indicates deployment with deployments A/a and C/c split due to sensor movement at MA/a3 and RC/C5, third indicates sensor number (see Figure 2). Sensors used to represent conditions at the shoreline (s), midreef flat (r), reef face (f), and offshore (o) are indicated; type: P denotes a Sea-Bird SBE26plus, PUV denotes a Nortek Aquadopp, and AUV a Nortek AWAC, depth: mean sensor depth during deployment; position: ~distance from the shore; burst sample: duration of 1 Hz sampling/time between burst samples, both in hours; site and time: experiment site and deployment time.

crest (Figure 2b and Table 1). The reef flat is relatively smooth and featureless other than loose rocks and occasional WWII paraphernalia. The smoothness of the reef likely is due to recementation of post-WWII demolition in which most of Roi-Namur was bulldozed and reutilized. The initial reef face slope is steep ( $\sim 0.08$ ) and composed of mild spur and groove features followed by a narrow terrace (near sensor 5) and increasingly irregular and rough topography (between sensors 5 and 7), all of which display a general lack of biota. We obtained the initial reef face slope estimate in a similar manner as at CMI from diver surveys and satellite images. Following the gradually sloping terraces is a rapid dropoff at the outer edge of the atoll near sensor 7. The tides at CMI and Roi are mixed semidiurnal/diurnal with a mean range of 1 m and a typical spring range of 1.6 m.

Site 3 lies on Guam (Figure 1c) a volcanic island at the southernmost end of the Mariana Islands archipelago. A cross-shore instrument array aligned along 95°N was deployed at Ipan reef on the southeast coast of Guam (Figure 1f). The reef flat at Ipan extends  $\sim 400$  m from a narrow sandy shore to the reef crest, and is relatively flat and featureless with an average depth of 0.5 m on the midreef flat during the experiment

(Figure 2c). The reef face, defined here as the region immediately seaward of the reef crest, is steep ( $\sim 0.06$  slope) with irregular and rough topography ranging from individual coral heads to boulders to spur and groove formations. The bathymetry at Ipan was collected by the Scanning Hydrographic Operational Airborne Lidar System (SHOALS). The quality of the SHOALS data is compromised within the breaker zone, hence we have less confidence of the bathymetry profile in this region (dashed curve in Figure 2c). The tides at Guam are mixed semidiurnal/diurnal with a mean range of 0.5 m and a typical spring tide range of 0.7 m. The reef flat usually is exposed during spring low tides.

The cross-shore arrays at each of the study sites consisted of bottom-mounted pressure sensors (Sea-Bird SBE26plus with Paroscientific Digiquartz pressure transducers) and combined pressure sensors (piezoelectric transducers) and acoustic Doppler current profilers (Nortek Aquadopp) (Figure 2 and Table 1). The profilers were set to measure one depth cell of 0.29–0.37 m width, centered 0.30–0.34 m above the bottom. At Roi and CMI, a Nortek Acoustic Wave and Current profiler (AWAC) was deployed in 13.8 m depth that measured pressure 1 m above the bottom, acoustic Doppler currents measured at a dynamically varying depth cell nominally 1 m below the surface, and acoustically tracked sea surface elevation. Data at CMI were collected between December 2009 and May 2010 (deployment MA), and at both CMI and Roi between November 2010 and May 2011 (deployments MC and RC, respectively). During two of the deployments (MA and RC), large wave events caused the reef face pressure sensors to shift to a different depth. These deployments are divided into two subdeployments of stable sensor positions (records after shifts denoted by Ma and Rc, see Table 1). At Ipan Guam, observations from three deployments during energetic wave conditions in the winter of 2008–2009 and the fall and winter of 2009–2010 are analyzed (deployments IL, IN, and IO).

All data were collected at 1 Hz sample frequency with different burst durations and intervals (Table 1). Pressure data with  $<0.1$  m of water over a sensor are not considered in our analysis. For the setup analysis at CMI and Roi, we focus largely on the Paroscientific Digiquartz P sensors, which exhibit less datum drift over time than the piezoelectric transducers. Sea surface elevation time series for wind waves are obtained indirectly using linear theory to depth correct the detided 15 min subrecords of bottom pressure, or directly in the case of the offshore AWAC sensors using acoustic surface tracking. The *rms* wave height,  $H$ , is computed over 15 min records as  $2\sqrt{2}\sigma$ , where  $\sigma$  is the standard deviation from the surface elevation spectrum integrated between 0.033 and 0.35 Hz for Roi and CMI, and 0.04 and 0.30 Hz for Ipan. At the deep offshore sensors at CMI and Roi (13.8 m), we compute  $H$  using the acoustically tracked sea surface elevation measurements.

Setup is computed following Vetter *et al.* [2010] from the 15 min average water depths,  $\bar{h}_i$ , where subscript  $i$  indicates sensor location. The setup at sensor  $i$  is the difference between  $\bar{h}_i$  and the reef face water level,  $\bar{h}_f$  (specific sensors identified in Table 1), as

$$\bar{\eta}_i = \bar{h}_i - \bar{h}_f - (bt + c) + \bar{\eta}_f, \quad (3)$$

where  $\bar{\eta}_f$  is the setdown at the reef face sensor,  $t$  is the time, and  $b$  and  $c$  are obtained from a least squares fit to account for relative pressure drift between the two sensors, and to select a reference level offset,  $c$ , so that  $\bar{\eta}_i = 0$  when the reef face excess *rms* wave height  $H_f - 1.2H_i = 0$ . This setup estimate differs from that in Vetter *et al.* [2010] in the determination of the reference offset  $c$ , which in Vetter *et al.* [2010] was estimated so that  $\bar{\eta}_i = 0$  when  $H_f = 0$ . The difference in  $c$  for the two offset corrections is negligible at Ipan; however, the larger tidal variations at CMI and Roi require accounting for the residual wave height in the setup estimate offset. Following Longuet-Higgins and Stewart [1962], setdown at the reef face sensor locations is estimated according to

$$\bar{\eta}_f = -\frac{H_f^2 k_f}{8 \sinh(2k_f \bar{h}_f)}, \quad (4)$$

where  $k_f$  is the wave number at the reef face sensor estimated from  $\bar{h}_f$ , the mean water level measured at the reef face, and the peak period,  $T_f$ . By including  $\bar{\eta}_f$  in (3),  $\bar{\eta}_i$  is referenced to the still water level and not to the reef face water level. We note, however, that  $\bar{\eta}_f$  is never  $<-0.06$  m for any of the deployments considered. We remark that setup estimates referenced to the AWACs (MC9, RC/c7) are similar to those estimates referenced to the reef face Seabirds (MC7, RC/c5) reported here.

### 3. Point Break Model

Solutions to (1) are obtained based on the point break assumption of Vetter *et al.* [2010]. Vetter *et al.* [2010] showed that an idealized point break model of wave transformation for normal incidence yields a setup formulation similar to Tait [1972], while avoiding the assumption of Tait [1972] that  $\gamma$  is constant across the surf zone. The point break model is motivated by visual observations that waves tend to break in a narrow zone on the reef face at the three study sites considered. To apply this approach to CMI and Roi, we must account for the nonnormal incidence of wind waves as they approach the reef. In Appendix A, we extend Vetter *et al.* [2010] to account for nonnormally incident waves.

For an idealized point break model of wave transformation (Appendix A2), Vetter *et al.* [2010, equation (13)] relate the difference between the setup on the reef flat,  $\bar{\eta}_r$ , and the setdown at the breakpoint,  $\bar{\eta}_b$ , to the difference between the wave height at breaking,  $H_b$ , and the residual wave height after breaking,  $H_r$ , according to

$$\bar{\eta}_r - \bar{\eta}_b = \frac{3}{8} \gamma_b (H_b - H_r), \quad (5)$$

where  $\gamma_b \equiv H_b/\bar{h}_b$ . In Vetter *et al.* [2010], both  $\gamma_b$  and  $H_r$  were assumed to be tidally independent. These assumptions followed both from the small tidal range at Ipan, and from the reef flat water level which controls  $H_r$  being setup dominated. The large tidal range at CMI and Roi and the longer deployments available for Ipan than considered by Vetter *et al.* [2010] allow for the assessment of the tidal dependence of the setup.

Equation (5), which assumes normal incidence, may be rewritten as

$$\bar{\eta}_i = p(h') H_b, \quad (6)$$

where

$$p(h') = \frac{5}{16} \gamma_b \left( 1 - 1.2 \frac{H_i}{H_b} \right). \quad (7)$$

In (6) and (7),  $\bar{\eta}_i$  and  $H_i$  are the setup and residual wave height at sensor  $i$  shoreward of the break point and  $h'$  is the tidal elevation. Equations (6) and (7) follow from equation (15) of Vetter *et al.* [2010] with  $\bar{\eta}_r$  and  $H_r$  replaced with  $\bar{\eta}_i$  and  $H_i$  therein. From (7), we see that the tidal elevation may affect the reef flat setup in two ways. First, as noted by Tait [1972] and others, the reef flat wave height  $H_i$  is tidally dependent through its dependence on total water level that includes both setup and tidal elevation. Second,  $\gamma_b$  may be tidally dependent through  $\bar{h}_b$  the water level at breaking. For nonnormal incidence, (6) and (7) generalize to

$$\bar{\eta}_i = p(h', \theta_b) H_b \quad (8)$$

(Appendix A) with

$$p(h', \theta_b) = \frac{1}{8} \left[ (2 \cos^2 \theta_b + 1) \frac{\Delta H_{ib}}{\bar{h}_b} - \frac{H_b}{2h_b} + \mathcal{B} \left( \frac{\Delta H_{ib}^2}{H_b} \log \bar{h}_b + \frac{H_i^2}{H_b} \log \frac{\bar{h}_i}{\bar{h}_b} \right) \right], \quad (9)$$

where  $\Delta H_{ib} \equiv H_b - H_i$  and

$$\mathcal{B} \equiv \frac{\sin^2 \theta(x)}{h(x)} = \frac{\sin^2 \theta_0}{h_0} \quad (10)$$

is a constant (independent of  $x$ ) assuming linear refraction and alongshore uniform bathymetry where  $h_0$  and  $\theta_0$  are a reference water level and wave angle. Equation (9) reduces to (7) for normal incidence ( $\theta_0 = \theta_b = 0$ ). In the estimation of  $\hat{\gamma}_b$  that follows, we apply (8) and (9) to the midreef sensor designated with  $i = r$  (see Table 1).

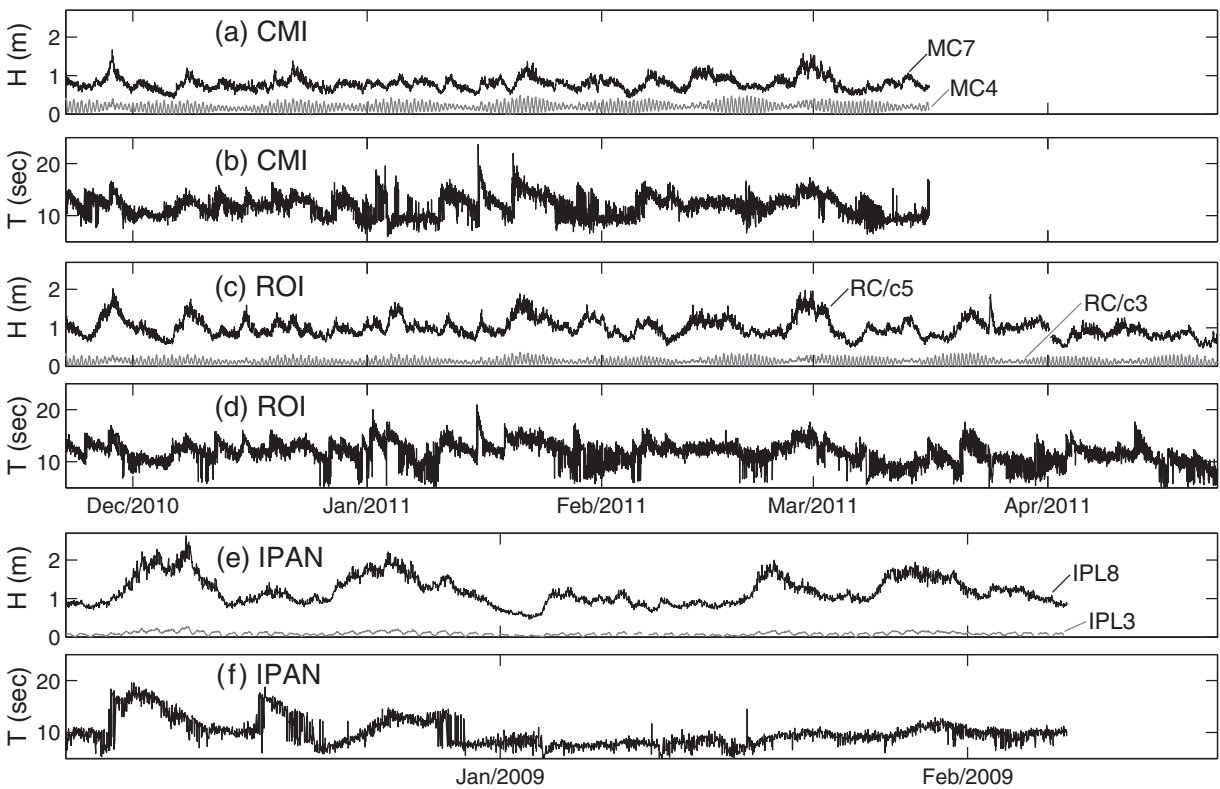


**Figure 3.** The incident *rms* wave heights at the reef face (MC7, RC/c5, IPL8) and reef flat sensors (MC4, RC/c3, IPL3) and the peak periods at CMI (a, b), Roi (c, d), and Ipan (e, f), respectively.

## 4. Results

### 4.1. Observations of Waves and Setup

Incident *rms* wave heights on the reef face at the three sites during the field experiments are typified by conditions during the MC, RC/c, and IL deployments. Wave heights and peak periods range from 0.4 to 1.7 m and 6.0 to 23.7 s, respectively, at CMI (Figures 3a and 3b), from 0.5 to 2.0 m and 4.3 to 20.9 s at Roi (Figures 3c and 3d), and from 0.5 to 2.6 m and 4.9 to 19.6 s at Ipan (Figures 3e and 3f). In contrast, reef flat *rms* wave heights are strongly depth limited shoreward of the surf zone, with a close resemblance to tidal elevation, particularly at CMI and Roi (Figures 3a and 3c), where the tidal range is twice as large as Ipan. The tendency for depth-limited wave heights on the reef flat also was described at Ipan by Vetter *et al.* [2010], with the local water level largely dominated by wave-driven setup.

The dependence of *rms* wave height on water level varies across the reef flat at each study site (Figure 4). A near linear relationship is observed at midreef sensors (MC4, Rc3, and IL3), with regression slopes estimated as 0.24 at CMI, 0.19 at Roi, and 0.21 at Ipan (Figure 4). Near the reef edge (MC6, Rc4, and IL5) the regression slope is higher than at midreef, which we attribute to incomplete saturation of wave heights in the surf zone. At inner reef sensors closer to shore at CMI (MC3 and MC2) and at Roi (RC1), wave heights tend to be higher for a given water level than at midreef. Both of these reef flats slope gently toward shore, which presumably promotes wave shoaling. The shoaling effect is not apparent over the more level reef flat at Ipan. The dependence of *rms* wave height to water level is noticeably more nonlinear at the inner reef than further offshore, particularly at Ipan (IL2 and IL1) and CMI (MC3 and MC2). We attribute this to frictional decay of waves being stronger at low water levels than at high. We also note that frictional effects are likely to be most noticeable at Ipan, the widest reef, and least at Roi, which has the smoothest reef flat substrate of the three sites.

The incident wave direction during the experiment departs significantly from shore normal at the RMI sites. The dominant wave direction is specified as the direction of peak energy obtained from directional spectral

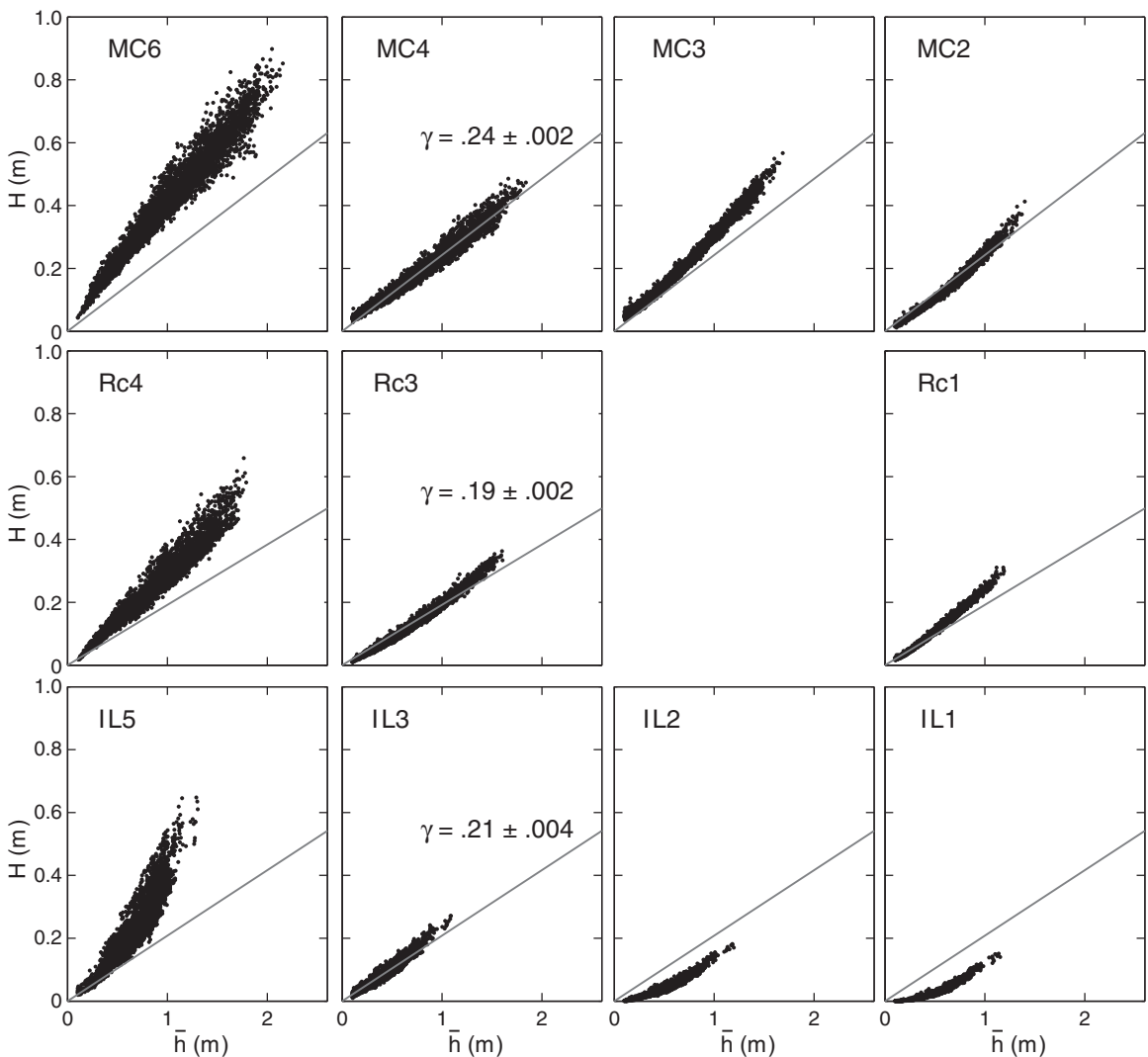


**Figure 4.** The *rms* wave height at the reef flat sensors as a function of the total water depth at each sensor. The gray lines in each plot are the zero intercept regression lines for sensors MC4, Rc3, and IL3 with regression coefficient  $\gamma = H_r / \bar{h}$ , indicated.

estimates using the deep (13.8 m) AUV sensors and the free software Directional WAve Spectra Toolbox version 1.3 (DIWASP). At CMI (MC9), the deployment averaged wave direction at the deepest sensor is  $\theta_o \sim 33^\circ$  of shore normal (Figure 5a). The wave field at CMI is dominated by trade wind waves and northwest swell waves that wrap around the north end of the atoll. At Roi, the deployment averaged wave arrival at the deepest sensor during the RC/c winter deployment is  $\theta_o \sim -57^\circ$  of shore normal (Figure 5b). The wave field at Roi during deployment C/c is dominated by winter swell from the northwest Pacific, with additional energy contributed by trade wind waves, which approach the shore at the reef face at nearly normal incidence. Just landward of the surf zone on the reef flats at CMI (MC6) and Roi (RC/c4), the wave direction is within  $10^\circ$  of shore normal (not shown), consistent with wave refraction assuming longshore uniform bathymetry. Linear refraction calculations also indicate that the deployment averaged angle of incidence at the reef face P sensors, RC/c5 and MC7, is  $\theta_f \sim -34^\circ$ , and  $\theta_f \sim 21^\circ$ , respectively. For Ipan deployments IN and IO (not shown), we find near normal (within  $10^\circ$ ) incidence at sensors on the reef face. Similar wave incident wave angles were reported by Pequignet *et al.* [2011] for the N deployment at Ipan. The shore normal incidence at Ipan is due to the prevalence of trade wind waves at this site. During deployments MA at CMI (only P sensors) and IL at Ipan (failure of a beam in the L9 sensor), we do not have direct estimates of the wave direction on the reef face. For later setup computations that require wave direction, we use the mean directions obtained from deployments MC and IO, which occurred during similar phases of the seasonal wave climatology as MA and IL.

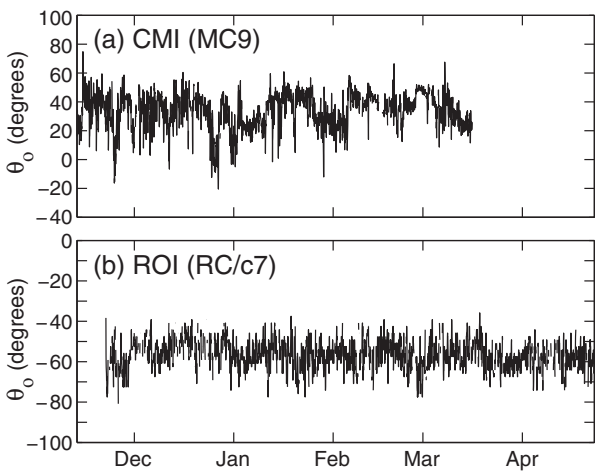


**Figure 5.** Dominant incident wave angle,  $\theta_o$ , every 3 h at approximately 13.8 m depth on the reef face for (a) CMI (MC9) and (b) ROI (RC/c7).  $\theta_o$  is specified as the direction of peak wave energy obtained from DIWASP derived directional wave spectra. The default maximum entropy methods (EMEP) in DIWASP was used for CMI, and the maximum likelihood estimator (EMLM) was used for ROI, which appeared to provide better separation of incident and reflected energy peaks at ROI where waves approach at more of a grazing angle than the other sites.

The estimated reef flat setup ( $\bar{\eta}_r$ ) at sensors MC4, RC/c3, and IL3,  $\bar{\eta}_r$ , is smaller in amplitude than tidal elevation changes at CMI and Roi (Figures 6a and 6b), and larger than the tidal elevation at Ipan (Figure 6c). Here we take the detrended water level at the fore reef sensor,  $h'_f$ , as a proxy of the tide, with weak nontidal sea level variations included. At all sites,  $\bar{\eta}_r$  exhibits a dependence on tidal elevation, with less setup observed at high tide than at low tide for a given incident wave height (Figure 7, top). The tidal dependence increases with increasing wave height. The largest tidal spread is observed at Roi, such that for a 1 m reef face wave height, setup on the reef flat is  $\sim 0.4$  m higher during peak low tide than peak high tide (Figure 7b). Although CMI has a similar tidal range as Roi, the largest wave events at CMI during deployment MC tended to occur at high tide. A similar

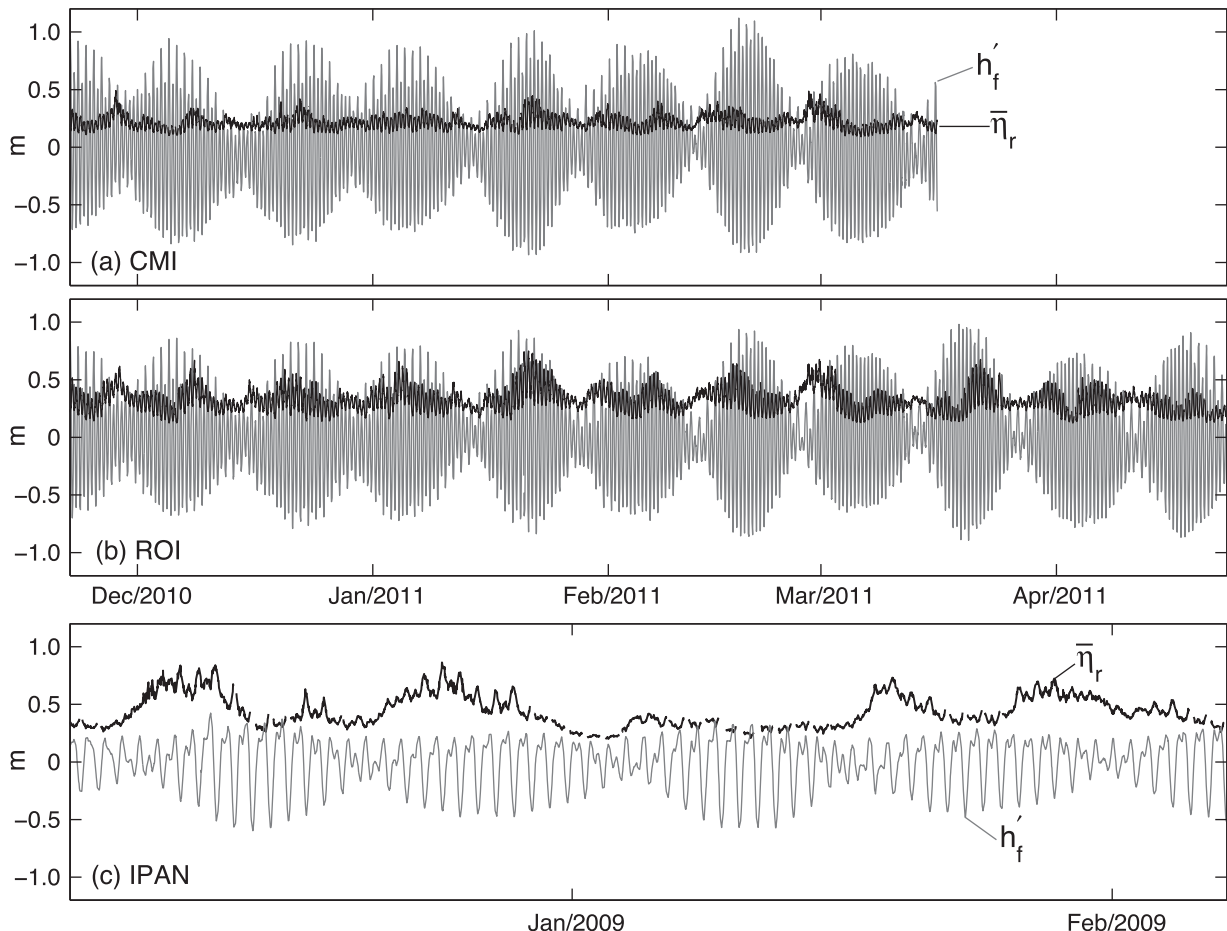


**Figure 6.** Time series of the tide ( $h'_f$ , gray) and reef flat setup ( $\bar{\eta}_r$ , black) at each of the sites.

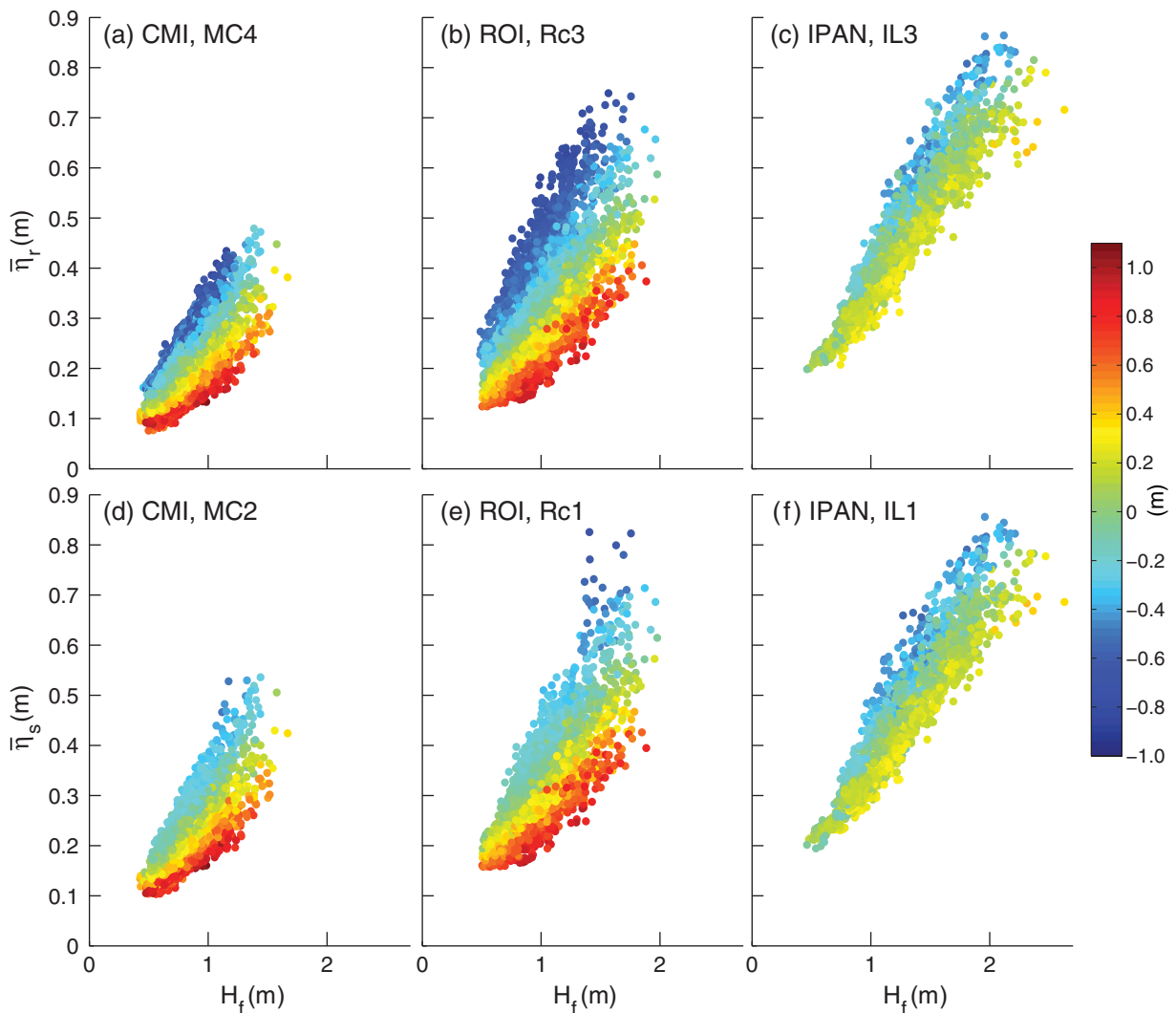


**Figure 7.** Setup (top) on the reef flat and (bottom) at the shore versus reef face wave height (MC7, RC/c5, IL8) colored with the tide,  $h'_f$ .

tidal dependence on setup was reported previously by Vetter *et al.* [2010] based on observations from Ipan (their Figure 9, G and N deployments) and at the island of Saipan (their Figure 11).

The estimated setup closest to the shoreline (Figure 7, bottom) shows a similar tidal dependence to setup estimates at the reef crest. Since the shoreline sensors tend to be exposed at low tide at Roi and CMI, the tidal variability of  $\bar{\eta}_s$  appears to be smaller than for  $\bar{\eta}_r$ . A linear regression analysis indicates that the observed setup amplitude is 16% and 11% higher near the shore (s) compared to the midreef (r) at CMI and Roi, respectively, while at Ipan the setup amplitude near the shore (s) is 2% lower than at midreef ((r), Figure 7, bottom). We evaluate cross-reef variations in setup in section 4.4. Recent studies at Ipan suggest that longshore water level gradients also are important on the reef flat, associated with wave-driven longshore flows directed toward a cross-reef channel south of the Ipan study site [Clarke, 2013]. Clarke [2013] found that longshore water level gradients associated with the flow increase predominantly south of our sensor array, and that order 10% reductions in setup amplitude may occur at the Ipan study site compared to sites further north in the far field of the channel. We emphasize that the tidal dependence of setup does not vary appreciably across the reef flat at any of the three sites.

#### 4.2. Setup Relative to Observed Reef Face Wave Heights

The tidal dependence of setup is assessed first by assuming that the observed reef face wave height ( $H_f$ ) approximates the breaking wave height, that  $\gamma_b$  is constant, and that the incident wave angle is shore

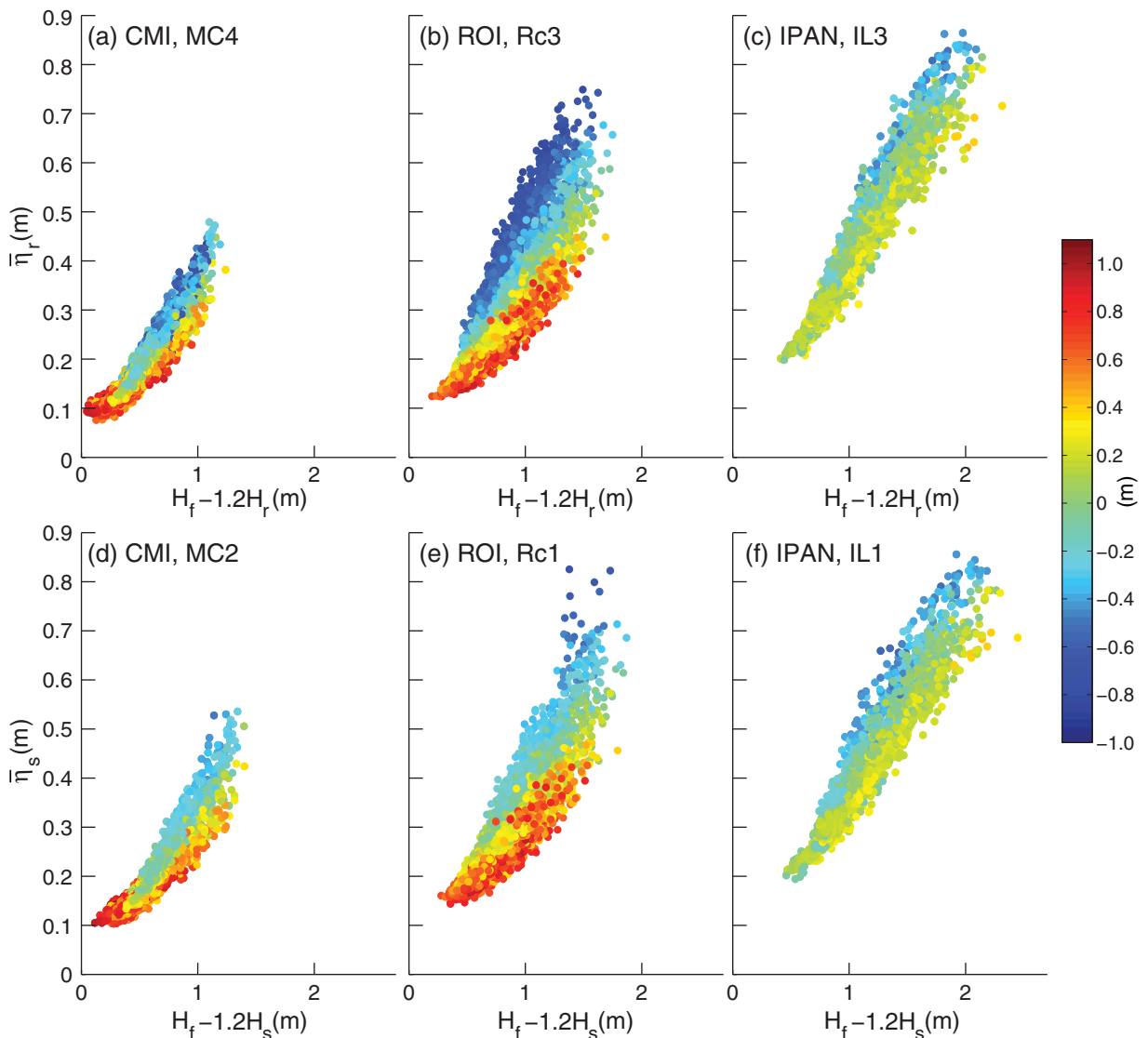


**Figure 8.** Setup (top) on the reef flat (top) and (bottom) at the shore versus excess wave height colored with the tide.

normal. Based on (6) and (7), we compare the observed setup  $\bar{\eta}_i$  on the reef flat ( $i = r$ , Figure 8, top) and near the shoreline ( $i = s$ , Figure 8, bottom) with the respective excess wave heights  $H_f - 1.2H_i$ . If the tidal dependence of setup is determined by the tidal dependence of  $H_i$  ( $i = r, s$ ), we would expect the scatter in Figure 8 to be reduced compared to Figure 7. The tidal dependence of setup is reduced at all sites, both at the shore and outer reef, most notably at CMI (Figures 8a and 8d). Nevertheless, the tidal dependence is still evident at each site, particularly at Roi, and we conclude that tidally dependent setup cannot be accounted for solely by a tidally varying residual wave height.

At all sites we find that the ratio of the observed setup at midreef to reef face wave height,  $\bar{\eta}_r / H_f$ , a measure of  $p(h')$  in (7), is highly correlated with the tidal elevation measured at the reef face,  $h'_r$  (Figure 9, left). To assess this empirical tidal dependence, we perform a linear regression of the form

$$\frac{\bar{\eta}_r}{H_f} = p_{11} h'_r + p_{01} \equiv p_1(h'_r) \quad (11)$$

and exclude data from the regressions with small excess wave heights ( $H_f - 1.2H_r < 0.4\text{m}$ ). This threshold excludes small waves that may not break on the reef face, particularly at high tide. For Roi which exhibits

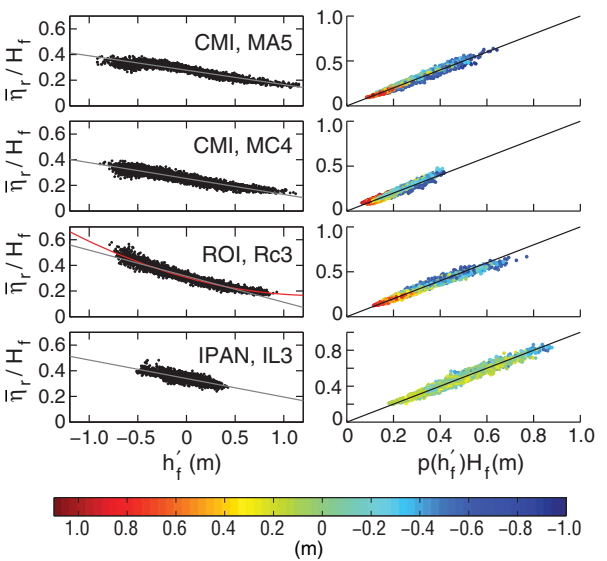


**Figure 9.** (left) The ratio of reef flat setup,  $\bar{\eta}_r$ , to reef face wave height,  $H_f$  (MA7, MC7, RC5, IL7, see Table 2), versus the tide,  $h'_f$ . The gray lines are the best fit linear regressions, while the red curve for Rc3 is the quadratic regression (Table 2). (right) Observed reef flat setup,  $\bar{\eta}_r$ , versus the reef face wave height,  $H_f$ , times the tidally dependent proportionality factor,  $p(h'_f)$  (Table 2) colored with the tide.

by (11) and (12) presented in Figure 9 (right). The tidal dependence of setup evident in Figures 7 and 8 is suppressed.

The regression coefficients obtained from (11) and (12) are significant at each of the sites (Table 2), with 95% confidence intervals obtained assuming independent data points at 12 h separations. Parameter differences between deployments are larger than the estimated standard errors for a single deployment. The linear regression accounts for approximately 90% of the variance at CMI and ROI. Only 35–60% of the variance is accounted for at Ipan by the regression, which may be related to the total water level being setup dominated at this site (Figure 6). For a given reef face wave height, the mean component ( $p_{0j}$ ) of  $\bar{\eta}_r/H_f$  is largest at Ipan (0.34–0.38), followed by ROI (0.31–0.33) and CMI (0.25–0.33). The sensitivity to tidal elevation is largest at ROI ( $p_{1j} \sim 0.20$ ), and smallest at CMI ( $p_{1j} \sim 0.13$ ).

#### 4.3. Setup Relative to Estimated Breaking Wave Heights

We use the point break model and the observations of reef flat setup,  $\bar{\eta}_r$ , to estimate the tidal dependence of  $\gamma_b$ . Equations (8) and (9) require time-varying estimates of the breaking wave height ( $H_b$ ), breaking water

**Table 2.** Estimates of  $p_1(h'_f)$ , (11), From Regressing the  $\bar{\eta}_r/H_f$  on the Tide,  $h'_f$ , Where  $\bar{\eta}_r$  is the Reef Flat Setup at Sensors MA/a5, MC4, RC/c3, IL3, IN3, and IO3, and  $H_f$  is the Reef Face Wave Height at Sensors MA/a7, MC7, RC/c5, IL7, IN7, and IO7<sup>a</sup>

Deployment	Order ( $j$ )	$R^2$	$p_{0j}$	$p_{1j}$	$p_{2j}$
MA	1	0.87	$0.28 \pm 0.002$	$-0.11 \pm 0.006$	
Ma	1	0.89	$0.33 \pm 0.003$	$-0.14 \pm 0.009$	
MC	1	0.88	$0.25 \pm 0.003$	$-0.12 \pm 0.007$	
RC	2	0.93	$0.31 \pm 0.005$	$-0.21 \pm 0.013$	$0.08 \pm 0.030$
RC	1	0.91	$0.32 \pm 0.004$	$-0.20 \pm 0.011$	
Rc	2	0.92	$0.31 \pm 0.005$	$-0.21 \pm 0.017$	$0.08 \pm 0.041$
Rc	1	0.90	$0.33 \pm 0.004$	$-0.20 \pm 0.012$	
IL	1	0.60	$0.34 \pm 0.004$	$-0.14 \pm 0.020$	
IN	1	0.35	$0.34 \pm 0.007$	$-0.16 \pm 0.046$	
IO	1	0.41	$0.38 \pm 0.003$	$-0.14 \pm 0.020$	

<sup>a</sup>Here and in Figure 9, we use the reef face sensor 7 for  $H_f$  for Ipan as it is deployed at a depth similar to the reef face sensors at CMI and ROI. Also quoted is the adjusted coefficient of determination,  $R^2$ , for each regression, and the quadratic regression coefficients  $p_2(h'_f)$ , (12), for ROI.

the strongest tidal dependence on setup, we find that a better fit to the data is obtained by a quadratic regression

$$\bar{\eta}_r = p_{22}h'_f^2 + p_{12}h'_f + p_{02} \equiv p_2(h'_f), \quad (12)$$

where in  $p_j$ , and the coefficients  $p_{ij}$ ,  $j$  is the order of the regression ( $j = 1$  for linear,  $= 2$  for quadratic). While the variance accounted for by the quadratic regression at ROI is only nominally larger than for the linear regression, the quadratic regression eliminates an obvious non-linear residual trend. The regressions  $p_j$  ( $j = 1$  for MA/MC and IL/N/O,  $j = 2$  for RC/c) account for a significant fraction of the residual scatter, which is evident in a comparison of the observed  $\bar{\eta}_r$  with those modeled

**Table 3.** Same as Table 2, but Replacing  $H_r$  With the Estimated Breaking Wave Height From the Iterative Approach,  $\hat{H}_b$ 

Deployment	Order ( $j$ )	$R^2$	$p_{0j}$	$p_{1j}$	$p_{2j}$
MA	1	0.78	$0.21 \pm 0.003$	$-0.09 \pm 0.007$	
Ma	1	0.85	$0.25 \pm 0.003$	$-0.10 \pm 0.008$	
MC	1	0.83	$0.19 \pm 0.002$	$-0.09 \pm 0.006$	
RC	2	0.94	$0.24 \pm 0.004$	$-0.14 \pm 0.012$	$0.05 \pm 0.029$
RC	1	0.92	$0.24 \pm 0.003$	$-0.14 \pm 0.010$	
Rc	2	0.93	$0.24 \pm 0.004$	$-0.14 \pm 0.012$	$0.05 \pm 0.028$
Rc	1	0.91	$0.25 \pm 0.003$	$-0.14 \pm 0.008$	
IL	1	0.57	$0.28 \pm 0.003$	$-0.11 \pm 0.015$	
IN	1	0.36	$0.25 \pm 0.005$	$-0.12 \pm 0.033$	
IO	1	0.41	$0.28 \pm 0.002$	$-0.10 \pm 0.014$	

depth ( $\bar{h}_b$ ), and the angle of incidence at breaking ( $\theta_b$ ), which are not measured directly. For normal incidence, (7) shows that the tidal dependence of the setup for the point break model is due in part to the residual wave height,  $H_r$ , and in part to  $\gamma_b$ . For nonnormal incidence, the tidal dependence of the setup is more complicated than (7) and we seek iterative estimates of  $\hat{H}_b$ ,  $\hat{h}_b$ , and  $\hat{\theta}_b$  to estimate  $\hat{\gamma}_b = \hat{H}_b / \hat{h}_b$ , where the caret denotes an estimate derived from the iterative model.

We start with the initial estimate for  $p(h_f, \theta_b) = p_j(h_f, \theta_f)$  (Table 2,  $j = 1$  for CMI and Ipan,  $j = 2$  for Roi) and solve (9) for a first approximation to  $\hat{h}_b$  using  $\hat{\theta}_b = \theta_f$ ,  $\hat{H}_b = H_f$ , and  $H_r$  and  $\bar{h}_r$  are the observed reef flat values therein. We next determine a first approximation to  $\hat{\theta}_b$  at  $\bar{h} = \hat{h}_b$  assuming linear refraction with longshore uniform bathymetry according to

$$\sin \theta(x) = \sqrt{\frac{\bar{h}(x)}{\bar{h}_f}} \sin \theta_f, \quad (13)$$

where  $\bar{h}_f$  and  $\theta_f$  are the (reference) 15 min average reef face water level and wave angle. We next invoke conservation of energy flux accounting for nonnormal incidence to obtain a first approximation to  $\hat{H}_b$  (i.e., we conservatively shoal  $H_r$  to the water depth of our first approximation to  $\hat{h}_b$ ). We then regress the ratio of our setup estimate to our first iterate of the breaking wave height,  $\bar{\eta}_r / \hat{H}_b$ , on the tide  $h'_f$  to obtain a second approximation to  $p(h'_f, \theta_b)$ . This procedure is repeated, and converges in approximately 12 iterations, yielding values of  $\hat{H}_b$  and  $\hat{h}_b$  that allow for the estimation of  $\hat{\gamma}_b$ . We note that while the deployment average reef face angles of incidence,  $\theta_f$  are  $-34^\circ$  and  $21^\circ$  for RC/c and MC, respectively, the estimated angles at breaking  $\hat{\theta}_b$  are  $-15^\circ$  and  $10^\circ$ .

The breaking wave height estimated from the iterative approach above is  $\sim 30\%$  larger than the observed reef face wave height ( $H_r$ ) at CMI and Ipan, and  $\sim 27\%$  higher at Roi where the observed angle of incidence is the largest. The regression coefficients of  $\bar{\eta}_r / \hat{H}_b$  on  $h'_f$  (Table 3) are similar to the coefficients obtained by regressing  $\bar{\eta}_r / H_r$  on  $h'_f$  (Table 2), with the tidal dependence of  $\bar{\eta}_r / \hat{H}_b$  largest at Roi. The mean components of the ratio,  $p_{0j}$ , at all sites are smaller using  $\hat{H}_b$  than  $H_r$  consistent with  $\hat{H}_b$  being larger than  $H_r$ . The mean component remains largest at Ipan and smallest at CMI. In addition, the tidal dependence is slightly less for  $\bar{\eta}_r / \hat{H}_b$  than for  $\bar{\eta}_r / H_r$  at each of the sites due to the ratio of the estimated breaking wave height to reef face wave height,  $\hat{H}_b / H_r$ , exhibiting weak tidal dependence, in particular for Roi.

#### 4.4. Tidal Dependence of Wave Breaking

We next consider the tidal dependence of  $\hat{\gamma}_b$  obtained from the iterative approach above. Figure 10 presents  $\hat{\gamma}_b$  as a function of the tide,  $h'_f$  where we exclude data for which  $\hat{h}_b - \bar{h}_r < 0.1$  m. For Ipan,  $\hat{h}_b - \bar{h}_r > 0.5$  m, even for small waves at high tide suggesting that breaking has occurred seaward of the reef flat reference sensor. For Roi and CMI,  $\hat{h}_b - \bar{h}_r > 0.1$  m for  $\sim 98\%$  and  $\sim 93\%$  of the observations, respectively. The incident wave heights are lower at CMI than at Roi and Ipan, however, the lower wave heights do not solely account for the larger percentage of  $\hat{h}_b - \bar{h}_r < 0.1$  m conditions observed at CMI. The mean and standard deviation of  $\hat{\gamma}_b$  range from  $0.80 \pm 0.06$  at CMI,  $0.95 \pm 0.14$  at Roi, and  $0.94 \pm 0.05$  at Ipan. The  $\hat{\gamma}_b$ 's at each site exhibit a tidal dependence such that  $\hat{\gamma}_b$  decreases at high tide and increases at low tide, matching the tidal dependence of the observed setup. The highest tidal range of  $\hat{\gamma}_b$  is observed at Roi.

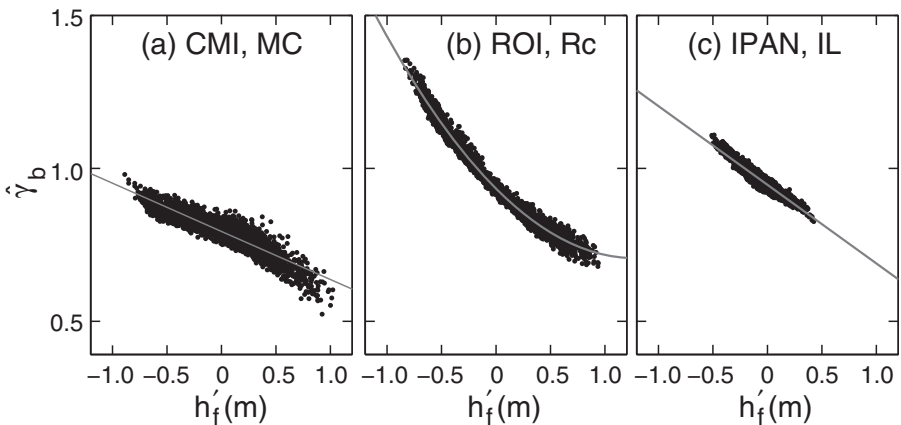


**Figure 10.** Tidal dependence of the breaking parameter,  $\hat{\gamma}_b = \hat{H}_b / \bar{h}_b$  estimated by the iterative method for the deployments indicated. The gray curves are the best fit linear regressions for CMI and Ipan, and the quadratic regression for Roi (Table 4).

(Figure 10). To quantify tidal dependence, we again regress  $\hat{\gamma}_b$  on tidal elevation (Figure 10 and Table 4) for CMI and Ipan (linear)

$$\hat{\gamma}_b = g_{11} h_f' + g_{01} \equiv g_1(h_f') \quad (14)$$

and for Roi (quadratic),

$$\hat{\gamma}_b = g_{22} h_f'^2 + g_{12} h_f' + g_{02} \equiv g_2(h_f'). \quad (15)$$

As was the case for the ratio of setup to reef face and breaking wave height (Tables 2 and 3), the strongest tidal dependence of  $\hat{\gamma}_b$  is observed at Roi, and the weakest at CMI (Table 4).

For Ipan (normal incidence  $\theta_f = 0$ ), we find  $\hat{\gamma}_b$  to be highly correlated with the tide with  $>90\%$  of the variance explained by the regression for deployments IL and IO. The tidal dependence of  $\hat{\gamma}_b$  is similar for all of the Ipan deployments, whereas the mean of  $\hat{\gamma}_b$  for deployment IN is  $\sim 10\%$  smaller than for deployments IL and IO (Table 4). As mentioned above, Vetter et al. [2010] estimated a constant (tidally independent) breaking parameter,  $\gamma_b$ , iteratively assuming conservation of energy flux on the reef face, (6) and (7) and assuming  $H_r$  constant. For Ipan deployments N and ManYi, Vetter et al. [2010] estimated  $\gamma_b$  as 0.9 and 1.1, respectively. We find that our iterative estimate of  $\hat{\gamma}_b$  ranges from 0.8 to 1.1 over the tidal range for deployments L and O, and from 0.7 to 1.0 for deployment N.

The  $\hat{\gamma}_b$ 's reported here agree qualitatively with the empirical relationship of Raubenheimer et al. [1996] between  $\gamma$  and bottom slope ( $\beta$ ), adjusted for rms wave height (Figure 11a). Our estimates of the mean bottom slope in the breaker zones at these sites range from 0.07 at Ipan, 0.09 at Roi, and 0.12 at CMI. The  $\hat{\gamma}_b$  at CMI is significantly lower than predicted, which may be due to an error in estimating the bottom slope in the breaker zone. The theoretical curve agrees well with the observed  $H_r / \bar{h}_r$  of 0.19 at Roi, 0.24 at CMI, and 0.21 at Ipan (Figure 4). Using  $\beta(k\bar{h}_b)^{-1}$  instead of  $\beta$  to estimate  $\gamma$  [Raubenheimer et al., 1996], where  $k$  is the

**Table 4.** Estimates of  $g_1$  (14) and  $g_2$  (15) From Regressing  $\hat{\gamma}_b$  onto the Tide,  $h_f'$ , Excluding Data for Which  $\bar{h}_b - \bar{h}_r < 0.1\text{m}$

Deployment	Order ( $j$ )	$R^2$	$g_{0j}$	$g_{1j}$	$g_{2j}$
MA	1	0.86	$0.86 \pm 0.004$	$-0.15 \pm 0.011$	
Ma	1	0.94	$1.01 \pm 0.004$	$-0.22 \pm 0.011$	
MC	1	0.86	$0.79 \pm 0.004$	$-0.16 \pm 0.011$	
RC	2	0.99	$0.89 \pm 0.006$	$-0.37 \pm 0.016$	$0.18 \pm 0.041$
RC	1	0.95	$0.92 \pm 0.006$	$-0.37 \pm 0.018$	
Rc	2	0.99	$0.93 \pm 0.004$	$-0.36 \pm 0.012$	$0.14 \pm 0.030$
Rc	1	0.96	$0.95 \pm 0.004$	$-0.35 \pm 0.011$	
IL	1	0.94	$0.95 \pm 0.002$	$-0.26 \pm 0.010$	
IN	1	0.78	$0.84 \pm 0.004$	$-0.27 \pm 0.029$	
IO	1	0.92	$0.92 \pm 0.002$	$-0.25 \pm 0.009$	

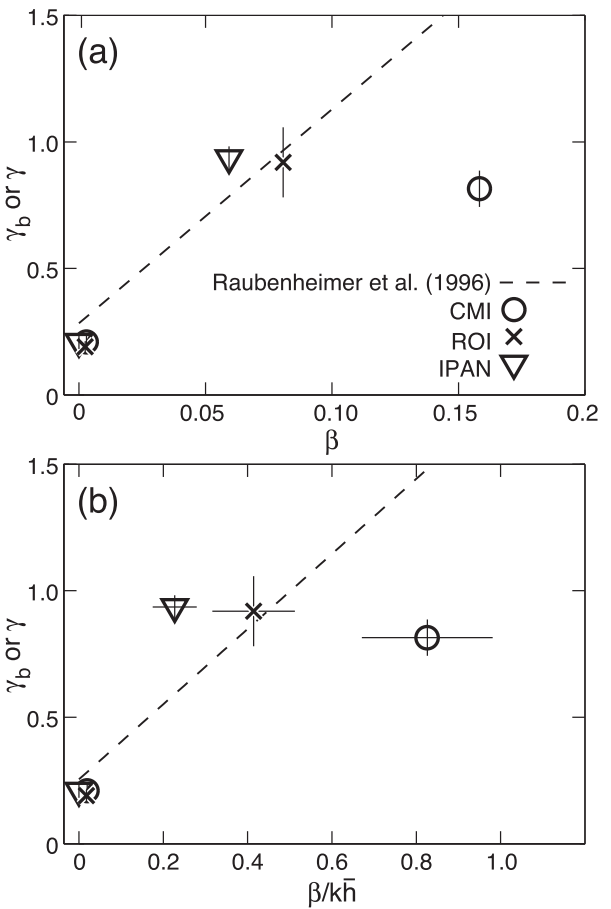


**Figure 11.** (a) Comparison of local bottom slope,  $\beta$ , versus  $\hat{\gamma}_b = \hat{H}_b/\bar{h}_b$  on the reef face and  $H/\bar{h}$  on the reef flat for the three study sites.  $\pm 1$  standard deviation ranges are depicted. The dashed line represents the analytical relationship of Raubenheimer et al. [1996],  $\gamma_b = (0.20 + 5.98\beta)(0.706)^{-1}$  (their Figure 7, adjusted for rms wave height). (b) is the same as Figure 11a except the abscissa is  $\beta$  divided by  $k\bar{h}$ , where  $k$  is the wave number of the dominant incident swell and  $\bar{h}$  is the total water depth, and the analytical relationship of Raubenheimer et al. [1996] is  $\gamma_b = (0.19 + 1.05\beta(k\bar{h})^{-1})(0.706)^{-1}$  (their Figure 9, adjusted for rms wave height) is included for comparison.

setup in part to a variable  $\gamma_b$ , but to extend this result to other island coastlines in a predictive sense, a physical understanding of the water level effect on setup is needed. We consider a number of possible explanations below; some are directly related to wave breaking, which we consider the more likely scenario, and some are not but their effects may be captured indirectly by a tidally dependent  $\gamma_b$ .

1. *Fixed breaker location*—Waves may break at a particular cross-shelf location on the reef face for a given wave height, regardless of tidal elevation. The fixed cross-shore position would cause the breaking depth to vary with tidal elevation. This would result in waves breaking in deeper water at high tide and shallower water at low tide, consistent with the sense of a tidally varying  $\gamma_b$ . If we subtract the tidal elevation from our estimate of  $\hat{h}_b$ , we find that the tidal variability of  $\hat{h}_b$  is reduced considerably at Roi, which supports a fixed break location regardless of tidal phase. The tendency is less apparent at CMI and Ipan. The different breaking behavior at Roi also may account for the nonlinear tidal dependence at Roi compared to CMI and Ipan (Figure 10).

2. *Topographic shape*—This explanation relies on a sensitivity of  $\gamma_b$  to bottom slope, similar to the description of Raubenheimer et al. [1996]. If the curvature of the reef face slope at these sites is concave down, then at low tide the break point for a given wave height would move further offshore where the local slope would increase given the topographic curvature, thus increasing  $\gamma_b$ . The opposite would occur at high tide

wave number of the dominant incident swell at the break point, does not improve the agreement with observed  $\hat{\gamma}_b$ .

Given our estimates of  $\hat{\gamma}_b$ , including the dependence on tidal elevation, we estimate setup across each reef flat using (6) and (7)

$$\hat{h}_i = \frac{5}{16} \hat{\gamma}_b (H_b - 1.2H_i). \quad (16)$$

The predicted and observed setup amplitudes agree well at all sensor locations with mean squared correlations of 0.92 (Figure 12). Changes in setup on the reef flat according to (6) and (7) are due to differences in reef flat wave heights (Figure 4). The agreement of predicted and observed setup at each of the sensor locations suggests that our estimates of  $\hat{\gamma}_b$  using only the midreef sensors are robust and provide a representative value of the similarity parameter at breaking. We illustrate the impact of using a  $\gamma_b$  that depends on water level compared to a constant  $\gamma_b$  following Vetter et al. [2010] using the empirical relationships for  $\gamma_b$  given in Table 4 and depicted in Figure 12. For a  $\pm 0.5$  m change in water level, the associated change in setup using the variable  $\gamma_b$  compared to the constant  $\gamma_b$  is  $\mp 9\%$  at CMI,  $\mp 14\%$  at Ipan, and  $-14\%, +24\%$  at Roi.

## 5. Discussion

We have related the tidal dependence of

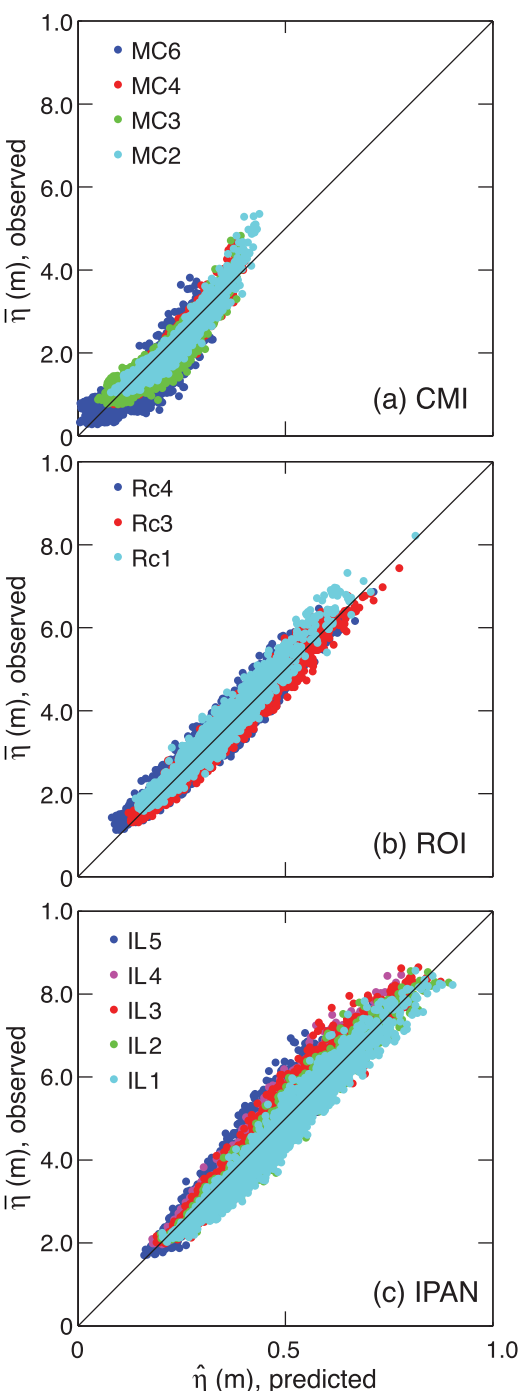


**Figure 12.** Predicted (16) versus observed setup for all sensor locations at (a) CMI ( $\hat{\gamma}_b = 0.83 - 0.15h'_f$ ), (b) Roi ( $\hat{\gamma}_b = 0.91 - 0.36h'_f + 0.16h'^2_f$ ), and (c) Ipan ( $\hat{\gamma}_b = 0.94 - 0.26h'_f$ ).

the estimated bottom stress component is small relative to the other terms in (1), and there is little sense of a tidal modulation to the offshore flow. Currents measured at the reef face at the RMI sites were made just below the surface, making it difficult to assess impacts on bottom stress.

We believe that some combination of the first two scenarios likely explains the inferred tidal dependence of  $\gamma_b$ , which all involve a tidal influence on the depth where the radiation stress forcing is applied in (1). Detailed measurements within the breaker zone are required to differentiate between these various

as the break point moved toward the reef crest. Although it appears likely from visual inspection that the surf zone bottom curvature is concave down at these sites, actual bathymetric measurements are not available for confirmation. Even a constant slope bathymetry through the reef face surf zone, however, could lead to tidally varying setup. Raubenheimer *et al.* [2001] found that the ratio of setup to offshore wave height should vary with  $\beta_{av}^{-1}$ , where  $\beta_{av}$  is the ratio of the average bottom depth of the surf zone to the surf zone width. Taking the reef face surf zone as extending from the single break point to the start of the reef platform, then  $\beta_{av}^{-1}$  will increase at low tide and decrease at high tide. The effect would be accentuated further with a concave down shaped bathymetric slope.

**3. Wave reflections**—A possible explanation is that wave reflections at the steep reef face vary with the tide, thus impacting the radiation stress gradient in the breaker zone. This seems unlikely as Pequignet *et al.* [2011] reported that <5% of the incident wind wave energy is reflected at the reef face at Ipan. Wave reflections are harder to assess at the RMI sites due to nonnormal incident waves; however, we see no indication of a tidal modulation to reflected wave energy. Weak reflected wave energy also has been measured in laboratory studies [Yao *et al.*, 2012] and assumed in modeling studies of wave transformation over steep reef faces [Massel and Gourlay, 2000]. Moreover, to explain the observed tidal dependence of setup, the reflected wave energy would have to be higher at high tide than at low tide, which seems unlikely given the greater transmitted energy onto the reef flat at high tide.

**4. Cross-shelf flows and bottom friction**—As noted by Symonds *et al.* [1995], Hearn [1999], Gourlay and Colleter [2005], and others, cross-shelf currents may contribute a bottom stress component to (1) that can affect the setup amplitude over reefs. If this component was to modulate with the tide, either by changes in current amplitude or in water depth [Hearn, 1999], this could introduce a tidal dependence to the setup amplitude. Wave-driven offshore currents are detected on the reef face, as described by Vetter *et al.* [2010] at Ipan; however,

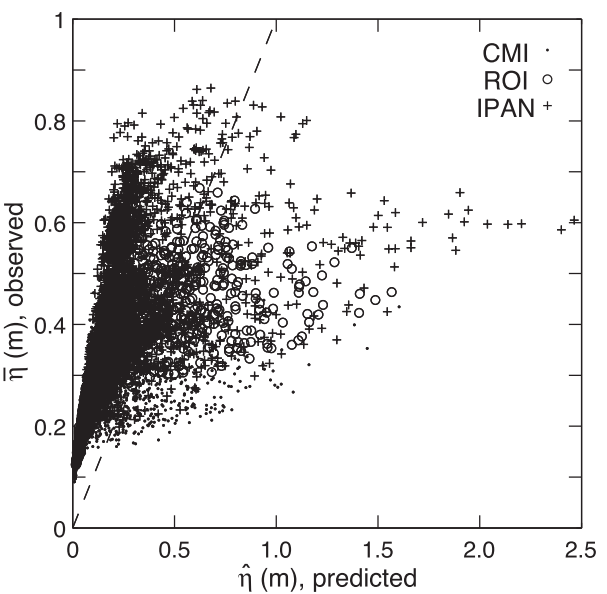


**Figure 13.** Predicted [Gourlay, 1996b, equation (8)] versus observed setup at the midreef sensors (CMI MC4, Roi Rc3, Ipan IL3). The dashed line represents a one-to-one relationship.

horizontal reef overpredicts the reef flat setup when breaking occurs seaward of the reef crest, as it does for the RMI and Ipan reefs. In these situations, (16) provides a more reliable estimate of fringing reef setup than the Gourlay [1996b] formulation.

The dependence of  $\gamma_b$  on water level for a fringing reef has been examined by Yao *et al.* [2012] based on laboratory experiments of monochromatic waves. They recommend a water level dependence (their equation (17)) that allows  $\gamma_b$  to transition from a maximum value on the sloping reef face to a minimum value on the reef flat, consistent with Figure 11. We note that the results of Yao *et al.* [2012] do not indicate a water level dependence of  $\gamma_b$  on the reef face, hence their expression does not account for the changes in  $\hat{\gamma}_b$  depicted in Figure 10.

## 6. Conclusions

Observations of breaking-wave setup on three fringing reefs reveal a strong tidal dependence (Figure 7). Applying an idealized point break model [Vetter *et al.*, 2010] generalized for nonnormal incidence (Appendix A), we attribute this tidal dependence in part to incomplete breaking [Tait, 1972] described by a total water level (setup and tide) dependent reef flat wave height,  $H_r$  (Figure 4). In addition, we demonstrate that the observed tidal dependence of the setup may be modeled by a tidally dependent breaking parameter,  $\gamma_b$ , defined as the ratio of wave height to water depth at the point break. We find that the large  $\gamma_b$ 's found for the three reef sites generally agree with slope-dependent estimates of  $\gamma$  reported in the literature [Raubenheimer *et al.*, 1996]. The tidal dependence of the setup is strongest at Roi and weakest at CMI, and we find that our estimated  $\hat{\gamma}_b$  derived from (8) and (9) also exhibits the largest and smallest tidal dependence at Roi and CMI. The tidal dependence of setup is observed across the reef flat; however, mean setup amplitudes increase from the midreef to the shoreline at Roi (~11% increase) and CMI (~16% increase), which is accounted for by changes in residual wave height (Figure 12). The observed setup tends to be more uniform across the reef flat at the Ipan site [Vetter *et al.*, 2010; Pequignet *et al.*, 2011].

Although the point break model is an idealization of breaking on the reef face, we believe that the underlying physical mechanism contributing to tidally dependent setup is captured by the model. That is, the depth of breaking modifies the strength of the radiation stress forcing in the setup balance (1). The point break model applies this at a single point, whereas more realistic transformation models will spread this

explanations. We further emphasize the importance of the depth where the radiation stress forcing is applied by considering setup estimates based on our observations using the analytic expression of Gourlay [1996b, equation (8)]. To apply this expression, we back-refract the rms wave height observed on the reef face to the deep ocean assuming normal incidence, which is consistent with the derivation of Gourlay [1996b] but inconsistent with the large observed angle of incidences observed at CMI and Roi (Figure 5). We also neglect wave reflections given the results of Pequignet *et al.* [2011]. We use a least squares fit to obtain estimates of the reef profile parameter ( $K_p$ ), which range from 0.10 to 0.16. The setup estimate based on Gourlay [1996b] departs significantly from the observed values, in particular for the largest setup predicted (Figure 13). As noted by Gourlay [1996b], his formulation based on an idealized horizontal reef overpredicts the reef flat setup when breaking occurs seaward of the reef crest, as it does for the RMI and Ipan reefs. In these situations, (16) provides a more reliable estimate of fringing reef setup than the Gourlay [1996b] formulation.

effect out across the breaker zone. In either case, the tidal influence on setup appears to result from breaking occurring in shallower water at low tide than at high tide for a given wave height.

Practical estimates of setup at fringing reefs based on (16) require estimates of  $\gamma_b$  and wave heights on the reef flat. Based on the results of this study, we recommend a value of  $\gamma_b$  based on reef face bottom slope following Raubenheimer *et al.* [1996]. Wave heights on the reef flat can be obtained approximately as  $H(x)=0.2(\bar{\eta}(x)+h(x))$ . Field observations are needed to estimate the water level dependence of  $\gamma_b$ ; however, lacking this information and using a constant  $\gamma_b$  likely results in an overestimate of setup at high tide or high sea level, which is a conservative estimate of maximum total water level. Application of (16) also requires an estimate of breaking wave height on the reef face.

Returning to our initial concerns regarding setup, coastal inundation, and sea level rise, it seems likely that rising sea level over a fixed reef topography will tend to diminish the setup contribution to shoreline water level changes similar to high tide conditions, due to higher water levels and wave heights on the reef flat and lower  $\gamma_b$ 's on the reef face. The decrease in the setup contribution to coastal water levels will be offset by stronger wind wave energy on the reef flat as the water level increases and potentially increased infra-gravity energy [Pequignet *et al.*, 2009].

## Appendix A

We here extend the simple theoretical argument of Vetter *et al.* [2010] to account for nonnormal incidence in the shallow water limit for longshore uniform dynamics and bathymetry. We start with conservation of cross-shore momentum [Longuet-Higgins and Stewart, 1962], (1) where

$$S_{xx} = \frac{E}{2} (2\cos^2\theta + 1). \quad (\text{A1})$$

We first consider the effects of nonnormal incidence on the idealized point break model of Vetter *et al.* [2010] for which the cross-shore profile of the wave height is

$$H(x) = (H_i - H_0(x))\mathcal{H}(x - x_b) + H_0(x) \quad x_0 < x < x_i \quad (\text{A2})$$

and  $\mathcal{H}$  is the Heaviside step function. In (A2),  $H_0(x)$  represents the incident wave height on the reef face seaward of the break point  $x_0 < x < x_b$ , and  $H_0(x_b) \equiv H_b$  defines the breaking wave height and  $H_i$  is the residual wave height at position  $x_i$  shoreward of the breakpoint. It is straightforward to show that

$$\frac{d\bar{\eta}}{dx} = -\frac{1}{\rho gh} \frac{dS_{xx}}{dx} = -\frac{1}{8h} \left[ (2\cos^2\theta + 1)H \frac{dH}{dx} - BH^2 \frac{d\bar{h}}{dx} \right], \quad (\text{A3})$$

where  $B$  is given by (10), and where

$$\frac{d}{dx}(\cos^2\theta) = -B \frac{d\bar{h}}{dx}. \quad (\text{A4})$$

Integrating (A3) from  $x_b$  to  $x_i$  shoreward of the break point, and invoking (A2), we find

$$\bar{\eta}_i - \bar{\eta}_b = \frac{1}{8} \left( [2\cos^2\theta_b + 1] \frac{H_b(H_b - H_i)}{\bar{h}_b} + \frac{\sin^2\theta_b}{\bar{h}_b} \left[ (H_b - H_i)^2 \log \bar{h}_b + H_i^2 \log(\bar{h}_i/\bar{h}_b) \right] \right). \quad (\text{A5})$$

For normal incidence at breaking ( $\theta_b = 0$ ), (A5) reduces to Vetter *et al.*'s [2010, (13)] (here (5)). It can be shown, following Longuet-Higgins and Stewart [1962], that the setdown in shallow water is independent of the angle of incidence, hence we obtain

$$\eta_i = p(h', \theta_b)H_b \quad (\text{A6})$$

where  $p(h', \theta_b)$  is given in (9).

## Acknowledgments

This work was supported through a grant from the National Science Foundation (OCE-0927407). Support for the Guam field experiment was provided by the U.S. Army Corps of Engineers via a subcontract through the University of California, San Diego as part of the PILOT project. Chris Kontoes, Carly Quisenberry, and Derek Young planned and executed the RMI field experiments. Additional field support was provided by Christine Pequignet, Paul Lethaby, Tyson Hilmer, Kimball Millikan, Lauren Tuthill, Chris Colgrove, Melanie Hutchinson, Chris Ostrander, and Bryan Rather. Don Hess at the College of the Marshall Islands and Jeff Pleadwell at Ipan, Guam provided logistical support. Jason Miller of the University of Guam Marine Laboratory provided invaluable assistance with the diving operation at Ipan. Anna Merrifield, Hyang Yoon, and Sarah Yasui assisted with the data processing. Documentation describing the DIWASP software toolbox is available at DIWASP, a directional wave spectra toolbox for MATLAB®: User Manual. Research Report WP-1601-DJ (V1.1), Centre for Water Research, University of Western Australia.

## References

- Apotsos, A., B. Raubenheimer, S. Elgar, R. T. Guza, and J. A. Smith (2007), Effects of wave rollers and bottom stress on wave setup, *J. Geophys. Res.*, 112, C02003, doi:10.1029/2006JC003549.
- Bowen, A. J., D. L. Inman, and V. P. Simmons (1968), Wave 'set-down' and set-up, *J. Geophys. Res.*, 73, 2569–2577.
- Clarke, S. J. (2013), The influence of a cross-reef channel on circulation over a fringing reef at Ipan, Guam, MS thesis, Honolulu, Univ. of Hawaii.
- Gerritsen, F. (1980), Wave attenuation and wave set-up on a coastal reef, in *Proceedings of the 17th International Conference on Coastal Engineering*, pp. 444, 461, Am. Soc. of Civ. Eng., Reston, Va.
- Gourlay, M. R. (1996a), Wave set-up on coral reefs. 1. Set-up and wave-generated flow on an idealised two dimensional reef, *Coastal Eng.*, 27, 161–193.
- Gourlay, M. R. (1996b), Wave set-up on coral reefs. 2. Set-up on reefs with various profiles, *Coastal Eng.*, 28, 17–55.
- Gourlay, M. R., and G. Gollerter (2005), Wave-generated flow on coral reefs—An analysis for two-dimensional horizontal reef-tops and steep faces, *Coastal Eng.*, 52, 353–387.
- Guza, R. T., and E. B. Thornton (1981), Wave set-up on a natural beach, *J. Geophys. Res.*, 86, 4133–4137.
- Hardy, T. A., and I. R. Young (1996), Field study of wave attenuation on an offshore coral reef, *J. Geophys. Res.*, 101, 14,311–14,326.
- Hearn, C. J. (1999), Wave-breaking hydrodynamics within coral reef systems and the effect of changing relative sea level, *J. Geophys. Res.*, 104, 30,007–30,019.
- Hench, J. L., J. J. Leichter, and S. G. Monismith (2008), Episodic circulation and exchange in a wave-driven coral reef and lagoon system, *Limnol. Oceanogr. Methods*, 53(6), 2681–2694.
- Holman, R. A., and A. H. Sallenger Jr. (1985), Setup and swash on a natural beach, *J. Geophys. Res.*, 90, 945–953.
- Hunter, J. (2012), A simple technique for estimating an allowance for uncertain sea-level rise, *Clim. Change*, 113(2), 239–252.
- Longuet-Higgins, M. S., and R. W. Stewart (1962), Radiation stress and mass transport in gravity waves, with application to surf-beats, *J. Fluid Mech.*, 13, 481–504.
- Lugo-Fernandez, A., H. H. Roberts, and W. J. Wiseman (1998), Tide effects on wave attenuation and wave set-up on a Caribbean coral reef, *Estuarine Coastal Shelf Sci.*, 47, 385–393.
- Massell, S. R., and M. R. Gourlay (2000), On the modeling of wave breaking and set-up on coral reefs, *Coastal Eng.*, 39, 1–27.
- Monismith, S. G., L. M. M. Herdman, S. Ahmerkamp, and J. L. Hench (2013), Wave transformation and wave-driven flow across a steep coral reef, *J. Phys. Oceanogr.*, 43, 1356–1379.
- Nielsen, P. (1988), Wave setup: A field study, *J. Geophys. Res.*, 93, 15,643–15,642.
- Nwogu, O., and Z. Demirbilek (2010), Infragravity wave motions and runup over shallow fringing reefs, *J. Waterw. Port Coastal Ocean Eng.*, 136, 295–305.
- Pequignet, A.-C., J. M. Becker, M. A. Merrifield, and J. Aucan (2009), Forcing of resonant modes on a fringing reef during tropical storm Man-Yi, *Geophys. Res. Lett.*, 36, L03607, doi:10.1029/2008GL036259.
- Pequignet, A.-C., J. M. Becker, M. A. Merrifield, and S. J. Boc (2011), The dissipation of wind wave energy across a fringing reef at Ipan, Guam, *Coral Reefs*, 30, 70–82.
- Raubenheimer, B., R. T. Guza, and S. Elgar (1996), Wave transformation across the inner surf zone, *J. Geophys. Res.*, 101, 25,589–25,597.
- Raubenheimer, B., R. T. Guza, and S. Elgar (2001), Field observations of wave-driven setdown and setup, *J. Geophys. Res.*, 106, 4629–4638.
- Seelig, W. (1983), Laboratory study of reef-lagoon system hydraulics, *J. Waterw. Port Coastal Ocean Eng.*, 109(4), 380–391.
- Seneviratne, S., et al. (2012), *Changes in Climate Extremes and their Impacts on the Natural Physical Environment, Managing the Risks of Extreme Events and Disasters to Advance Climate Change Adaptation (SREX)*, pp. 109–230, Intergovernmental Panel on Climate Change, Cambridge, U.K.
- Solomon, S., D. Qin, M. Manning, Z. Chen, M. Marquis, K. B. Averyt, M. Tignor, and H. L. Miller (Eds.) (2007), *Climate Change 2007: The Physical Science Basis*, 940 pp., Cambridge Univ. Press, Cambridge, U. K.
- Su, S.-F., A. Sheremet, and J. M. Smith (2011), Parametric wave-breaking on steep reefs, *Coastal Engineering Proceedings*, 1(32), doi: 10.9753/icce.v32.waves.16.
- Symonds, G., K. P. Black, and I. R. Young (1995), Wave-driven flow over shallow reefs, *J. Geophys. Res.*, 100, 2639–2648.
- Taebi, S., R. J. Lowe, C. B. Pattiaratchi, G. N. Ivey, G. Symonds, and R. Brinkman (2011), Nearshore circulation in a tropical fringing reef system, *J. Geophys. Res.*, 116, C02016, doi:10.1029/2010JC006439.
- Tait, R. J. (1972), Wave set-up on coral reefs, *J. Geophys. Res.*, 77(12), 2207–2211.
- Van Dongeren, A., R. Lowe, A. Pomeroy, D. M. Tran, D. Roelvink, G. Symonds, and R. Ranasinghe (2013), Numerical modeling of low-frequency wave dynamics over a fringing coral reef, *Coastal Eng.*, 73, 178–190.
- Vetter, O., J. M. Becker, M. A. Merrifield, A.-C. Pequignet, J. Aucan, S. Boc, and C. Pollard (2010), Wave set-up over a Pacific Island fringing reef, *J. Geophys. Res.*, 115, C12066, doi:10.1029/2010JC006455.
- Yao, Y., Z. Huang, S. G. Monismith, and E. Y. M. Lo (2012), Characteristics of monochromatic wave breaking over fringing reefs, *J. Coastal Res.*, 29(1), 94–104.
- Young, I. R. (1989), Wave transformations on coral reefs, *J. Geophys. Res.*, 94, 9779–9789.

## Erratum

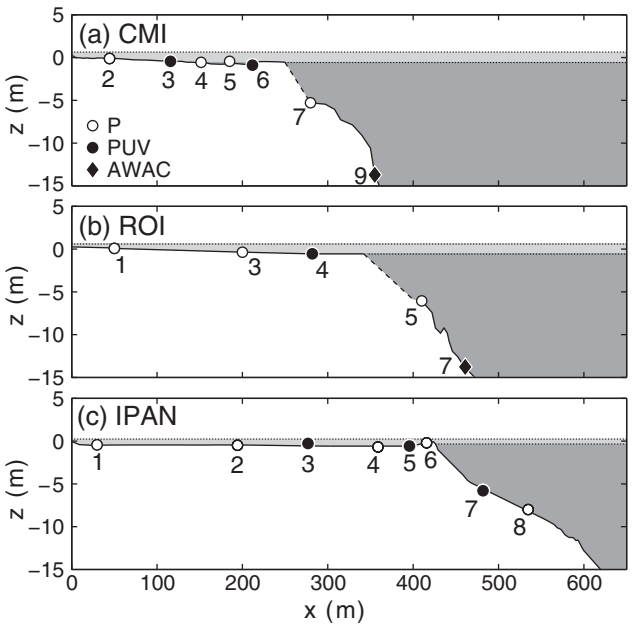
The originally published version of this article contained errors that are corrected here.

Most of the errors in the original manuscript involved reported wave angles, which arose due to a manufacturer error in the AWAC processing software. The processing error occurred in the Nortek software that converts raw binary files to ASCII WAD files. If the option “include velocity time” is selected, the program produces slant beam velocities regardless of the user selected reference frame, which in our case was meant to be east, north, and up (ENU). The main results of the paper are not affected greatly; however, the wave angle corrections result in changes to a number of estimated parameters. With the software error corrected, we now estimate the dominant incident wave angle at MC9 and RC/c7 from the flux in the sea and swell band rather than from the DIWASP package. We include the corrected Figure 5 and caption below, and here describe the corrections to the angles reported in the text of the original version of the manuscript. At CMI (MC9) the deployment averaged wave direction is  $\theta_0 = 6^\circ$  (instead of  $\theta_0 = 33^\circ$ ) and at Roi (RC/c7)  $\theta_0 = 9^\circ$  (instead of  $\theta_0 = -54^\circ$ ). The deployment averaged angle of incidence at the reef face P sensors RC/c5 and MC7 is  $\theta_f = 6^\circ$  (instead of  $\theta_f = -34^\circ$ ) and  $\theta_f = 4^\circ$  (instead of  $\theta_f = 21^\circ$ ), respectively. The deployment averaged angles at breaking reported in §4.3 for RC/c5 and MC7 are  $\theta_b = 4^\circ$  (instead of  $\theta_b = -15^\circ$ ) and  $\theta_b = 3^\circ$  (instead of  $\theta_b = 10^\circ$ ), respectively. The corrected angles have a small effect on the estimates of  $\hat{\gamma}_b$  in §4.4 for Roi and CMI, and the corrected Table 4 is included below. In the first paragraph in §4.4, the mean and standard deviation of  $\hat{\gamma}_b$  now range from  $0.77 \pm 0.06$  at CMI, and from  $0.86 \pm 0.13$  at Roi. Also, at the end of §4.4, for a  $\pm 0.5$  m change in water level, the associated change in setup using the variable  $\gamma_b$  compared to the constant  $\gamma_b$  now is  $-17\%$ ,  $+25\%$  at Roi. Changes to Figure 12 using the new values of  $\hat{\gamma}_b$  are not discernible, and the caption to Figure 12 should read (a) CMI (MC,  $\hat{\gamma}_b = 0.79 - 0.15 h'_f$ ) and (b) Roi (RC,  $\hat{\gamma}_b = 0.84 - 0.35 h'_f + 0.15 h'^2_f$ ).

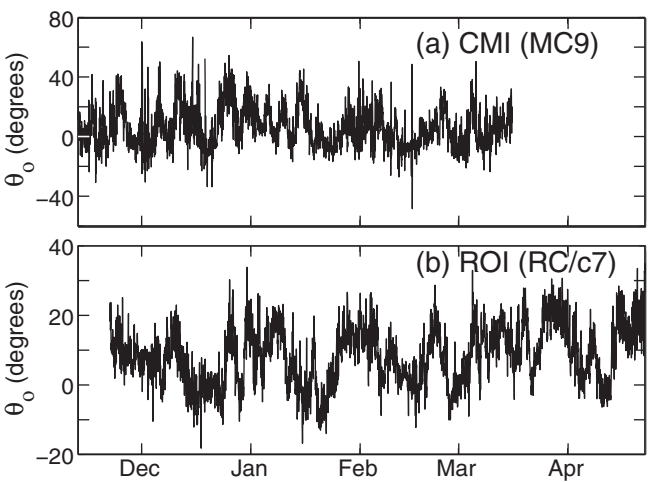
Two additional errors were discovered. The bottom panel of the original Figure 2 showed an incorrect profile at Ipan. The corrected Figure 2 is included below. The final correction to the original manuscript is due to a mistake converting *rms* to significant wave height. The corrected Figure 11 is included below with the correct caption. Additionally, in the text in §4.4, the statement that “the  $\hat{\gamma}_b$  at CMI is significantly lower than predicted” should read “the  $\hat{\gamma}_b$ ’s at Roi and Ipan are significantly higher than predicted”.

**Corrected Table 4.** Estimates of  $g_1$  (14) and  $g_2$  (15) From Regressing  $\hat{\gamma}_b$  on to the Tide,  $h'_f$  Excluding Data for Which  $\bar{h}_b - \bar{h}_r < 0.1$  m

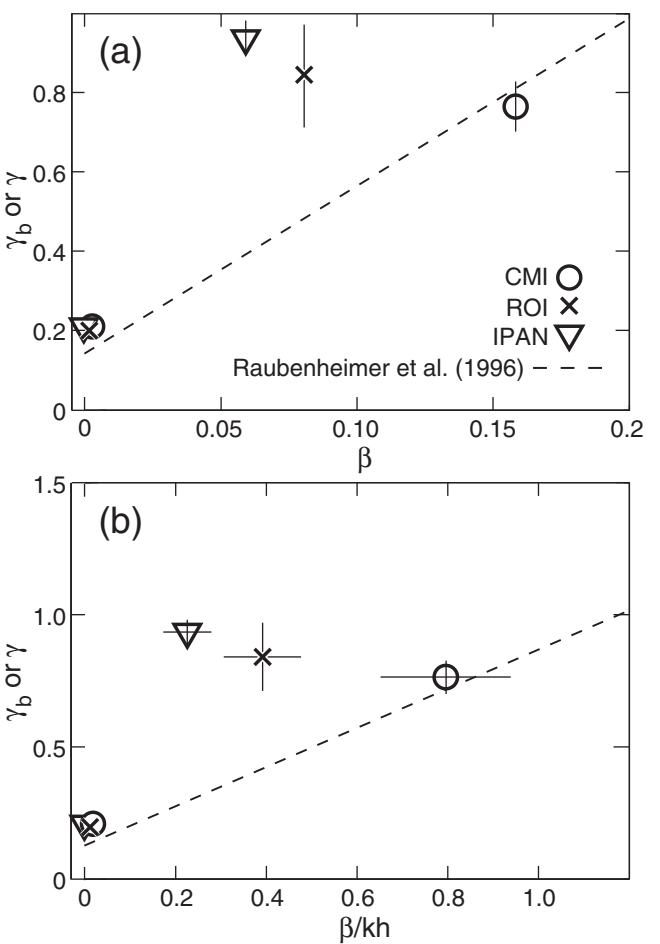
Deployment	Order ( <i>j</i> )	$R^2$	$g_{0j}$	$g_{1j}$	$g_{2j}$
MA	1	0.87	$0.82 \pm 0.004$	$-0.15 \pm 0.009$	
Ma	1	0.94	$0.98 \pm 0.003$	$-0.21 \pm 0.009$	
MC	1	0.89	$0.76 \pm 0.003$	$-0.16 \pm 0.009$	
RC	2	0.99	$0.82 \pm 0.004$	$-0.35 \pm 0.011$	$0.16 \pm 0.025$
RC	1	0.95	$0.84 \pm 0.005$	$-0.34 \pm 0.013$	
Rc	2	0.99	$0.86 \pm 0.002$	$-0.34 \pm 0.008$	$0.14 \pm 0.019$
Rc	1	0.95	$0.88 \pm 0.003$	$-0.33 \pm 0.008$	
IL	1	0.94	$0.95 \pm 0.002$	$-0.26 \pm 0.010$	
IN	1	0.78	$0.84 \pm 0.004$	$-0.27 \pm 0.029$	
IO	1	0.92	$0.92 \pm 0.002$	$-0.25 \pm 0.009$	



**Corrected Figure 2.** The reef bathymetry and sensor locations (P - Sea-Bird SBE 27plus, PUV -Aquadopp, AWAC) for (a) CMI, (b) Roi, and (c) Ipan are presented as a function of cross-shore distance ( $x$ , positive offshore). During deployment A/a at CMI, the mid-reef Seabird (MA/a5) is located between sensors MC6 and MC4 (see Table 1). The dashed sections of the bathymetry curves indicate locations where wave conditions prevented direct depth measurements and linear interpolation between known points is made. The band of water levels at the surface represents mean lower low water (MLLW, bottom of light band) and mean higher high water (MHHW, top of light band), computed for the duration of the C (CMI and Roi) and L (Ipan) deployments.



**Corrected Figure 5.** Dominant incident wave angle,  $\theta_0$ , every 3 hours at approximately 13.8m depth on the reef face for (a) CMI (MC9) and (b) ROI (RC/c7).  $\theta_0$  is specified as the direction of peak wave energy flux in the sea and swell band.



**Corrected Figure 11.** (a) Comparison of local bottom slope,  $\beta$ , versus  $\hat{\gamma}_b = \hat{H}_b / \hat{h}_b$  on the reef face and  $H/h$  on the reef flat for the three study sites.  $\pm 1$  standard deviation ranges are depicted. The dashed line represents the analytical relationship of Raubenheimer et al. [1996],  $\hat{\gamma}_b = (0.20 + 5.98\beta)(0.706)$  (their Figure 7, adjusted for rms wave height). (b) is the same as (a) except the abscissa is  $\beta$  divided by  $kh$ , where  $k$  is the wavenumber of the dominant incident swell and  $h$  is water depth, and the analytical relationship of Raubenheimer et al. [1996] is  $\hat{\gamma}_b = (0.19 + 1.05\beta(kh)^{-1})(0.706)$  (their Figure 9, adjusted for rms wave height) is included for comparison.